九州大学学術情報リポジトリ
Kyushu University Institutional Repository

Study on VHF Plasma Characteristics by Laser Thomson Scattering

陳，韋廷

https://doi.org/10.15017/1398402

出版情報：九州大学, 2013, 博士（工学）, 課程博士
バージョン：
権利関係：全文ファイル公表済

Study on VHF Plasma Characteristics by Laser Thomson Scattering

Weiting CHEN

Department of Applied Science for Electronics and Materials

Interdisciplinary Graduate School of Engineering Sciences

Kyushu University

September, 2013

Contents

Acknowledgements

Chapter 1

General Introduction

1.1 Introduction 1

1.2 Aim of this study 5

1.3 Outline of the thesis 6

References 8

Chapter 2

VHF Plasma and Diagnostics

2.1 Overview of solar cell 10

2.2 Plasma diagnostic techniques 14

2.3 VHF plasma 16

2.3.1 Electron trapping effect 16

2.3.2 Power absorption 19

2.4 Power feeding 19

2.5 Laser scattering 23

2.5.1 Laser Thomson scattering 23

2.5.2 Rayleigh scattering 29

2.5.3 Stray light 29

2.5.4 Experimental setup of LTS system ……………………………32
2.6 Langmuir probe method ……………………………………………...39
2.6.1 Characterization of the probe …….……………………………39
2.6.2 Construction of the probe ………………………………………45
2.7 Simulation ………………………………………………………………47
2.7.1 Description of the model ………………………………………48
References ……………………………………………………………………..51

Chapter 3

Diagnostics of VHF Argon Plasmas by Laser Thomson Scattering

3.1 Introduction …………………………………………………………..53
3.2 Experimental setup …………………………………………………...54
3.3 Results and discussion.. ……………………………………………....59
3.4 Summary ……………………………………………………………..67
References …………………………………………………………………68

Chapter 4

Investigation of VHF Argon Plasma at High Pressure by Balanced Power Feeding

4.1 Introduction …………………………………………………………..69
4.2 Results and discussion.. ……………………………………………...71

4.2.1 Comparison of conventional and balanced power feeding……..71
4.2.2 Comparison of results by LTS method and probe method……..79
4.2.3 Simulation……………………………………………………....79
4.3 Summary ……………………………………………………………..87
References ……………………………………………………………….88

Chapter 5

Conclusion

5.1 Summary of this study ………………………………………………89
5.2 Suggestions for the future work ……………………………………...90

Acknowledgements

This research was conducted at the Ionized Gas and Laser Research Laboratory of Kyushu University. Many people have contributed directly and indirectly to the success of my research during my stay in Japan.

First of all, I am extremely grateful to my advisor, Prof. Kiichiro Uchino for giving me the great opportunity of joining his research group, many valuable suggestions, encouragement through the course of this work, critical reading of the manuscript, and useful advices. Also I would like to express my sincere appreciation to Associate Prof. Yukihiko Yamagata, Assistant Prof. Kentaro Tomita, and Assistant Prof. Ogiwara for their continuous guidance, active help, discussion, and encouragement during the whole investigation.

I am highly grateful to Prof. Reiji Hattori and Associate Prof. Naoji Yamamoto for serving on my thesis committee and providing constructive criticism.

Moreover, I would also like to thank Prof. Yoshinobu Kawai for his guidance and assistance in getting my graduate career. He gave me many advices on not only research but also life during my study. I would like to acknowledge Dr. Hiromu Takatsuka and Dr. Yoshiaki Takeuchi of Mitsubishi Heavy Industry for the technical support and valuable discussion during my study.

I am very grateful for the friendship of all of the members in Uchino Lab., in particular, Mr. Bolouki Nima, Mr. Koichiro Koge, Mr. Ryota Komatsu and Mr. Naoki Kimura for their technical support and discussion in this study.

Finally, I wish especially thank my parents and brother for their constant love, encouragement, understanding, and academically or financially support. This allows me to focus on the research and study. I would like to dedicate this thesis to them.

Chapter 1
General Introduction

1.1 Introduction

Ever since the industrial revolution, the use of fossil fuel has become indispensable in our life. The continuous emission of carbon dioxide into our atmosphere has drastically affected the earth. Results of the rising of sea level and unusual weather change have been proved to be due to global warming. Therefore, technologies with low environmental impact and zero "greenhouse gas" emissions are likely to be of increasing importance over the coming decades. Among them, solar has its advantages than others: it is free, clean, more secure, with minimal maintenance required, and produces minimal environmental impact.

Historically, crystalline silicon (c-Si) has been used as the light-absorbing semiconductor in most solar cells, even though it is a relatively poor absorber of light and requires a considerable thickness (several hundred microns) of material. Nevertheless, it has proved convenient because it yields stable solar cells with good efficiencies (15-18%) and uses process technology developed from the huge knowledge base of microelectronics industry. The high cost of crystalline silicon wafers (they make up 40-50% of the cost of a finished module) has led the industry to look at cheaper materials to make solar cells. The selected materials are all strong light absorbers and need to be about 1 micron thickness, so materials costs must be significantly reduced. The most common materials are amorphous silicon (a-Si), or polycrystalline materials which including microcrystalline silicon (μc-Si).

Hydrogenated amorphous silicon (a-SiH) is usually prepared by RF discharge plasma CVD where the parallel plate type electrodes and the frequency of 13.56 MHz are conventionally used. Although in this case the increase in the deposition rate is achieved by increasing the power of the RF source, the deposition rate is at most 0.2-0.3 nm/sec. Recently, a further improvement toward faster, uniform deposition has been demanded from the industrial perspective of productivity improvements of the products. So far, several researchers have reported the method for generating a high density plasma using frequencies higher than 13.56 MHz [1-5], i.e., the method for increasing the deposition rate by applying very high frequency (VHF) to the plasma CVD and this method has drawn attention because it can produce relatively high-quality films at a high speed. In fact, Curtins et al. [1] achieved 2 nm/sec at 70 MHz. These results were confirmed by other researchers [4-5]. However, the costs of amorphous silicon solar cell are relatively expensive compared with the crystalline silicon solar cells because of low conversion efficiency.

In order to increase the conversion efficiency, Shah et al [6] proposed a "tandem" thin film solar cell consisting of a microcrystalline silicon solar bottom cell and an amorphous silicon top cell. Microcrystalline silicon (μc-Si:H) is an attractive low band gap absorber material for integration in thin-film solar cells [7-8]. Now the tandem thin film solar cells are very popular and the efficiency of around 11 % with the area of 1 m x 1 m was recently reported. The structure of the tandem thin film solar cell is described in Chap. 2. However, the costs of the tandem thin film solar cells are still high compared with that of the crystalline silicon solar cells. The cost of the thin film solar cells strongly depends on both the efficiency and the deposition rate. Thus, it is the most important subject in the development of silicon thin film solar cells to prepare μc-Si:H

with high deposition rates. Now the industry requires at least 1 nm/s as the deposition rate.

Recently, it was found [7-8] that higher deposition rate of μc-Si:H is achieved by a narrow gap discharge at high pressure, maintaining the high quality. This method is called "high pressure depletion method" and widely used. However, the mechanism has not been understood. Paschen's law suggests that the higher the pressure becomes, the shorter the distance between the electrodes for discharge should be. As a result, discharge voltages will be greater because of larger losses of plasma to the electrodes. As well known, the deposition rate is proportional to the electron density. Lower electron temperature is required for the fabrication of high quality thin films because the ion bombardment energy is proportional to the electron temperature. Thus, it is one of the most important subjects in the production of microcrystalline silicon solar cells to examine the characteristics of a VHF plasma at high pressure.

As already described, the plasma CVD technology using the VHF plasma provides high quality silicon thin films with a high deposition rate. However, there are few research groups to measure the characteristics of the VHF plasma at high pressure because of the difficulty of the diagnostics. Kawai et al [9] produced a VHF hydrogen plasma with a ladder shaped electrode and found that when the power source frequency is increased, the electron density n_e increases and the electron temperature T_e decreases: n_e~1.6 x 10 ^{16} (m^{-3}) and T_e~2 eV at 200 MHz for 100 mTorr. In their experiments, the Langmuir probe was used to measure the plasma parameters. Yamauchi et al [10] attempted to measure the plasma parameters of a VHF hydrogen plasma (frequency:60 MHz) with a short gap discharge (gap distance = 5-10 mm) at high pressures and showed that the electron density takes a peak value at a certain pressure and the electron

temperature is around 10 eV that is relatively high. Recently Nishimiya et al [11] measured the characteristics of a VHF S_iH_4/H_2 plasma at high pressures by a heated Langmuir probe and found out the same tendency as that of the VHF H_2 plasma.

It is also one of the important subjects for the cost reduction of solar cells to produce a large area VHF plasma (> 1 m^2). Takatsuka et al [12] succeeded in producing a uniform VHF SiH_4/H_2 plasma (frequency: 60 MHz) over 1.1 m x 1.4 m using a multi rod electrode and obtained 2.5 nm/s as the deposition rate. Schmidt et al [13] attempted the improvement of plasma uniformity using a Gaussian-lens electrode for compensating the standing wave effects for VHF plasmas in the large area reactors, where the power source frequency was up to 100 MHz. They obtained plasma uniformity of ±10 % for the argon plasma (frequency: 67.8 MHz). In this case, the uniformity was estimated from the ion saturation current of the Langmuir probe. On the other hand, there are some companies to produce a large area silicon thin film solar cells using a conventional CVD (frequency: 13.56 MHz), but their deposition rates were lower than 1 nm/s.

As already described, the characteristics of a VHF plasma have been examined with the Langmuir probe, so far. However, when the probe is inserted, the VHF plasma produced by a narrow gap discharge is seriously disturbed and may change the parameters such as the density and temperature of electrons. In addition, the probe theory is not used at high pressures because the ion mean-free path is much shorter than the sheath length [14]. Thus, it is strongly expected to develop diagnostics that do not disturb VHF discharges at high pressures. We have been trying to measure the characteristics of the VHF plasma by the laser Thomson scattering (LTS) method.

In this thesis, we have been applying LTS to various discharge plasmas. In order to

support the validity of the results of LTS measurements, we compared the values of the electron density and electron temperature at different plasma conditions measured by LTS and the Langmuir probe. Microcrystalline silicon is fabricated by introducing a small amount of S_iH_4 gas into a H_2 plasma, so that the parameters of the S_iH_4/H_2 plasma are considered to be similar to those of the H_2 plasma. On the other hand, the electron density in the H_2 plasma is lower than 10^{16} m^{-3}, so that we have examined the characteristics of the argon plasma by LTS.

Besides the experimental study, to simulate the VHF argon plasma using the Plasma Hybrid Module (PHM) of PEGASUS software was proposed [15]. We examined the dependences of the VHF argon plasma produced by the balanced power feeding method on the applied voltage. By comparison of those results with the LTS method, we can ensure the reliability of the plasma simulation.

1.2 Aim of this study

The aim of this thesis is to study the characteristics of the VHF plasma at high pressures by LTS. First, the laser disturbance of the argon plasma is considered because it was reported [16] that the Thomson scattering signal from the xenon plasma was affected by the photo-ionization of metastable xenon atoms when LTS experiments are performed with laser power densities of > 10^{15} W/m^2 [16]. After examining the applicability of LTS to the diagnostics of VHF argon plasmas, the values of the electron density and electron temperature measured by LTS and the Langmuir probe are compared. These results may support the validity of the results of LTS measurements. Furthermore, the dependence of the VHF plasma parameters on the pressure and the VHF power by using the LTS method are examined, where the VHF plasma is produced by the balanced power feeding method and the conventional power feeding method.

Finally, the simulate of the VHF plasma using the PHM of PEGASUS software is tried. Simulation results are compared with the experimental results measured by LTS in order to confirm the reliability of the simulation.

1.3 Outline of the thesis

The thesis is divided into five chapters as briefly summarized in the following.

Chapter 1 is the introduction.

Chapter 2 includes a general introduction of the solar cell, the principle of the VHF plasma, power feeding methods, the experimental setup, and plasma diagnostic systems. The diagnostics of the VHF plasma used in this study included the LTS method, and Langmuir probe method. Also the simulation model of the VHF plasma using the PHM of PEGASUS software is described.

Chapter 3 describes the development of the LTS method as the diagnostics of the VHF argon plasmas. The effect of the photo-ionization of metastable atoms on the Thomson scattering spectrum was examined by comparing the spectra obtained with a plano-convex lens and a cylindrical lens. By reducing the power density of the YAG laser below 1×10^{13} W/m^2, the removal of the influence of the photo-ionization of metastable argon atoms on the Thomson scattering spectrum of the VHF argon plasma was succeeded. Therefore, these results support the validity of LTS measurements.

Chapter 4 describes the dependence of the VHF plasma parameters on the various conditions where a VHF plasma was produced by a balanced power feeding method and a conventional power feeding method. Compared with the conventional power feeding method, n_e and T_e by the balanced power feeding method showed the outstanding performance not only on the dependence of the pressure but also on the power. In addition, the pressure dependences of the plasma parameters at high pressure were

examined by LTS method and Langmuir probe method. It was found that the n_e values measured by the Langmuir probe method showed the different tendency from the values measured by the LTS method at high pressure. This indicated that the Langmuir probe method was not reliable for high pressures at around 1 Torr. Besides, we simulated the VHF argon plasma using the PHM of PEGASUS software. The n_e and T_e values were not so much different from those measured by the LTS method. Then, it was concluded that both LTS diagnostics and the simulation can be powerful tools to study VHF plasmas.

Finally, chapter 5 includes conclusions and suggestions for future work.

References

[1] H. Curtins, N. Wyrsch, M. Favre and A. V. Shah, Plasma Chem. Plasma Process. **7**, 267 (1987).

[2] S. Oda, J. Noda and M. Matsumura, Jpn. J. Appl. Phys. **29**, 1889(1990).

[3] A. A. Howling, J.-L. Dorier , Ch. Hollenstein, U. Kroll and F. Finger, J. Vac. Sci. & Technol. A, **10**, 1080 (1992).

[4] M.Heintze, R.Zedlitz and G. H. Bauer: J. Phys.D, Appl. Phys. **26**, 1781 (1993).

[5] M.Heintze and R.Zedlitz, J. Non-Cryst. Solids **198-200**, 1038 (1996).

[6] A. Shah, J. Meier, E. Vallat-Sauvain, C. Droz, U. Kroll, N. Wyrsch, J. Guillet, U. Graf, Thin Solid Films 403 –404 (2002) 179–187.

[7] M. Kondo, M. Fukawa, L. Guo and A. Matsuda, J. Non-Cryst. Solids, 266-269, 84 (2000).

[8] U. Graf, J. Meier, U. Kroll, J. Bailat, C. Droz, E. Vallat-Sauvain and A. Shah, Thin Solid Films, 427, 37 (2003).

[9] Y. Kawai, M. Yoshioka, T. Yamane, Y. Takeuchi, M. Murata, Surface & Coating Technology, 116-119, 662 (1999).

[10] Y. Yamauchi, Y. Takeuchi, H. Takatsuka, H. Yamashita, H. Muta, Y. Kawai, Contrib. Plasma Phys., 48, 326 (2008).

[11] T. Nishimiya, T. Yamane, S. Nakao, Y. Takeuchi, Y. Yamauchi, H. Takatsuka, H. Muta, K. Uchino, Y. Kawai, Surface & Coating Technology, 205, S 411 (2011).

[12] H. Takatsuka, M. Noda, Y. Yonekura, Y. Takeuchi, Y. Yamauchi, Solar Energy, 77, 951 (2004).

[13] H. Schmidt, L. Sansonnens, A. A. Howling, Ch. Hollenstein, M. Elyaakoubi, J. P. M. Schmitt, J. Appl. Phys., 95, 4559 (2004).

[14] T. E. Sheridan and J. Goree, Phys. Fluids B **3**, 4, 326 (2008).

[15] PEGASUS Software Inc., http://www.psinc.co.jp/english/index.html.

[16] N. Yamamoto, K. Tomita, K. Sugita, T. Kurita, H. Nakashima, and K. Uchino, Rev. Sci. Instrum., **83**, 073106 (2012).

Chapter 2
VHF Plasma and Diagnostics

2.1 Overview of solar cell

Sterling and Swann [1] were the first to publish the formation of films of ”silicon from silane” in a radio frequency glow discharge in 1965. The amorphous layers showed an extremely high resistivity. In 1969, Chittick et al. [2] prepared amorphous silicon in the same manner and found that it had better photoconductive properties than that made by the traditional techniques, evaporation and sputtering. Their papers also contain the first report on the possibility of doping the material substitutionally. In the same years, also the first low temperature microcrystalline silicon layers were deposited on glass substrates by Veprek and Marecek who used hydrogen plasma and a chemical transport method at 600°C in 1968. Until 1974, Lewis et al. [3] showed that the electronic defect density in amorphous germanium prepared by sputtering could be reduced by adding hydrogen to the plasma. Next year, Triska et al. [4] showed by means of an evolution experiment that also amorphous silicon deposited by glow discharge from pure silane did contain hydrogen. Thus electronic grade amorphous silicon is in fact an alloy of silicon and hydrogen, and was since then called hydrogenated amorphous silicon (a-Si:H). Compared to a-Si:H that absorbs light from 300 nm to 750 nm, μc-Si:H absorbs light coming from a wider spectral range, extending up from 300 nm to 1100 nm. Furthermore, the μc-Si:H solar cell is reported to be largely stable against light induced degradation [5].

Many solar cell researches have concentrated on increasing the efficiency and reducing the cost, thus making solar cells commercially viable. The solar cell efficiency

is defined as the ratio of the electrical output of a solar cell to the incident energy in the form of sunlight. One possibility for reducing cost significantly is the development of thin film solar cell technologies. Most photovoltaic solar technologies rely on semiconductor grade crystalline silicon wafers, which are expensive to produce compared with energy from fossil fuel source. In order to reduce high materials cost, thin film technologies are developed.

The conversion efficiency of thin film solar cell is lower than other kinds of solar cell, such as CIS, CIGS, etc. So, it is very important to research how to develop higher conversion efficiency, leading to the cost reduction of the silicon thin film solar cells. As already describe in Chap. 1, the "tandem" thin film solar cell that Shah et al [6] proposed is one of the promising candidates for the cost reduction of the silicon thin film solar cells. Therefore, the optical combination of these two materials takes advantage of larger part of the solar spectrum and the conversion efficiency of the incident light into electricity can be consequently improved. A combination of a- Si solar cell and μc-Si solar cell is called double junction solar cell or tandem solar cell. It has been reported in some researches and references [7-8].

The typical tandem solar cell is shown in the Fig. 2.3. Compare with single junction solar cell, the top cell (amorphous silicon p-i-n) combined to the structure. Producing a tandem cell is not an easy task, largely due to the thin properties of the materials and the difficulties putting up the current between the layers. These cells are much more difficult to produce because the electrical characteristics of each layer have to be carefully matched. In particular, the photocurrent generated in each layer needs to be matched; otherwise electrons will be absorbed between layers. In the case of those following problem, theoretically, the optical combination of these two materials takes

advantage absorption of larger part of the solar spectrum and the conversion efficiency of the incident light into electricity can be consequently improved.

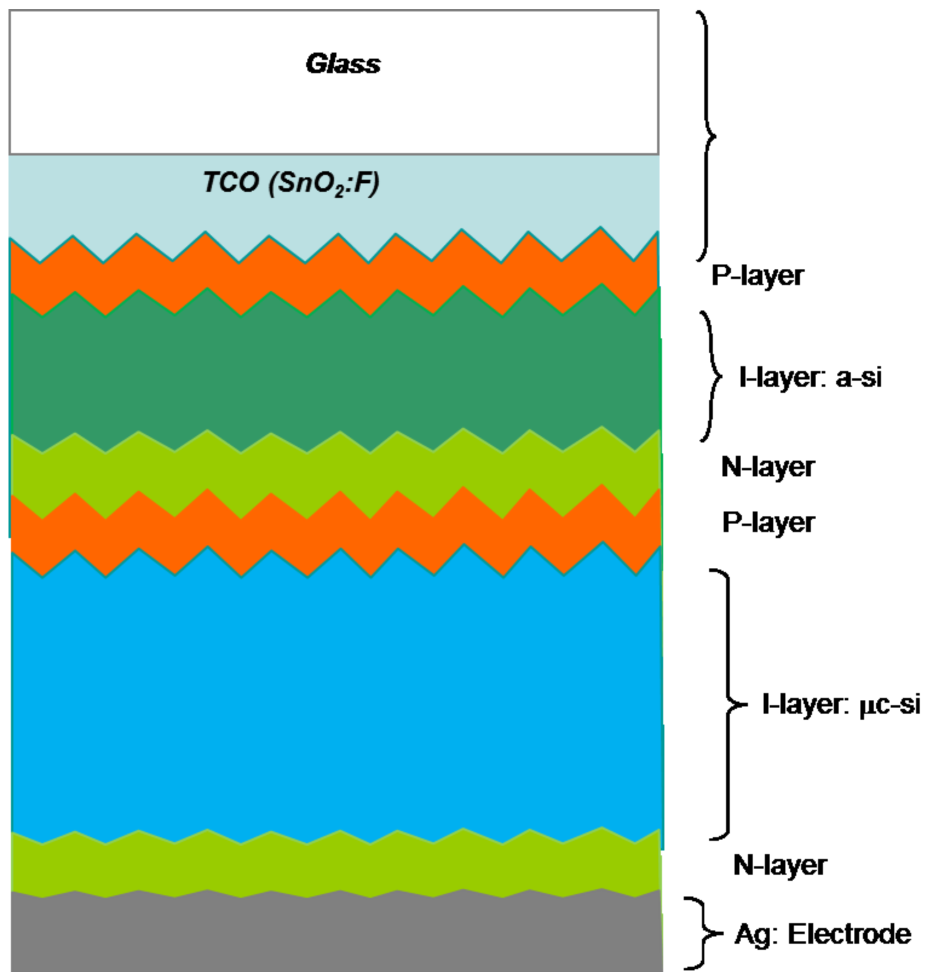

Fig. 2.3 The typical tandem solar cell.

2.2 Plasma diagnostic techniques

The diagnostics of the plasma properties are crucial for understanding physical and chemical processes which take place in the plasma processing. Plasma diagnostics is an extensive branch of plasma science and lots of mechanisms are required to discuss it in details. There are several techniques to analyze electron properties of the plasmas. Each method has its particular advantages and disadvantages. Some of the techniques are mentioned below.

The Langmuir probe method can be used to investigate the characteristics of VHF plasmas, such as the electron density n_e and the electron temperature T_e, and electron energy distribution function (EEDF). A Langmuir probe is one of the most frequently used and useful diagnostic tool in plasma physics due to its simplicity of the design, fabrication and easy to move. It provides the information regarding various plasma parameters, rather than volume averaged results which are obtained by other techniques such as microwave interferometry. Details of Langmuir probe method are explained in Sec. 2.6.

Microwave interferometry is a well-established diagnostic technique which is used to measure both the time averaged and time dependent electron line density [9-11]. If a microwave signal is passed through an auxiliary reference path and nulled against that of the signal through a measurement path when a plasma is absent, the effect of striking a plasma within the measurement path is to cause a phase shift in the output signal. This phase shift is proportional to the integrated line density of electrons. Compared to the Langmuir probe, it is a non-invasive technique. The theory behind its operation is not complicated and subject to less misinterpretation. This technique measures the line average electron density and the radial and the axial distribution of the electron density

should be known in order to infer the localized electron density. And the information of the EEDF is not obtained from the technique.

In this thesis, we focus on the active diagnostics such as laser scattering. Laser scattering such as laser Thomson scattering (LTS) and Rayleigh scattering, can provide a substantial amount of accurate information about plasma parameters such as electron density, electron temperature, and EEDF. LTS is a very attractive technique to measure the plasma parameters and to verify results measured from other diagnostic techniques, because it is relatively non-intrusive, the interpretation of the measured results is straightforward and assumptions on the plasma parameters are in principle not necessary. Also, those parameters are obtained as local values with high spatial and temporal resolutions. We describe about LTS in Sec. 2.5.

2.3 VHF plasma

2.3.1 Electron trapping effect

A VHF plasma is a kind of non-thermal plasmas which are produced at pressures ≤ 10 Torr. In the VHF plasma, electrons are heated up to a temperature of several eV, while ions and neutral particles remain at low temperatures which are close to the temperature of the chamber wall. This non-equilibrium feature is suitable for the plasma processing. The VHF plasma is characterized by electron trapping, that is, discharge frequency should satisfy the following condition:

$$f_{pi} << f < f_{pe} \tag{2.1}$$

Here f is the discharge frequency, and f_{pi} and f_{pe} is the plasma frequency of ions and electrons, respectively. In addition, the electron displacement δ_x should be shorter than a spacing gap between discharge electrodes for $\omega << \upsilon_m$ [12]:

$$\delta x = \frac{qE_0}{m_e \omega \upsilon_m} << \frac{d}{2} \tag{2.2}$$

Here d is a spacing gap between discharge electrodes, ω and υ_m is the angular frequency of VHF power source and electron collision frequency, respectively, and q, m_e and E_0 is electron charge, electron mass and the amplitude of the VHF electric field. As shown in Fig. 2.4, electron trapping effect provides better confinement of electrons and as a result the electron density becomes high. Thus, the electron density is considered to peak at a certain condition where electron trapping is most effective. The Eq. (2.2) indicates that E_0 and υ_m are important parameters in a VHF plasma, that is, the VHF power and pressure are key parameters in the VHF plasma characteristics. When the VHF power is increased, the amplitude of the electron oscillation in the VHF electric field E_0 increases and as a result the condition for electron trapping, $\delta x << d/2$, is not valid. Therefore, to

increase υ_m by increasing the pressure is required for VHF plasma discharges at high powers.

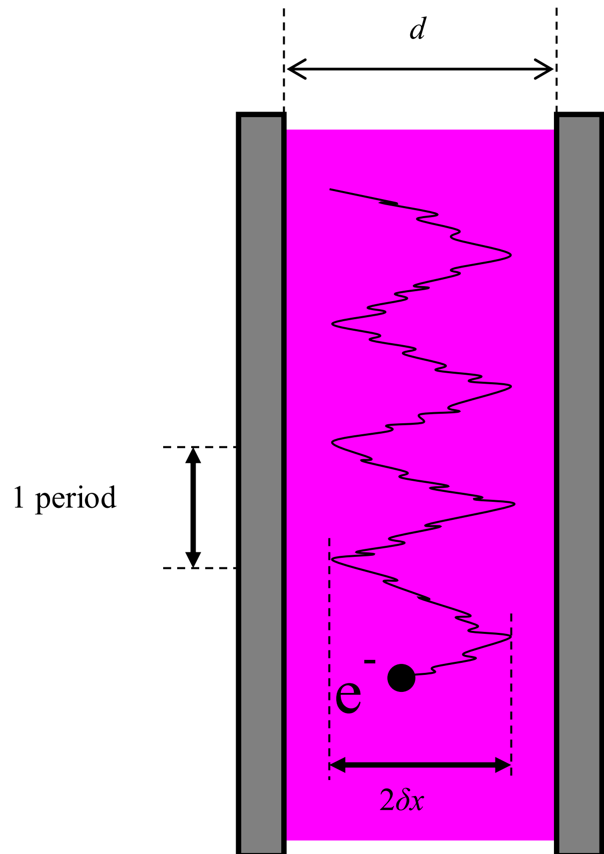

Fig. 2.4 Schematic diagram of electron trapping effect.

2.3.2 Power absorption

We can estimate the mean power density P_{abs} of the discharge supplied by the electric fields E_0 using the diffusion-controlled model [12-13]. The mean power density absorbed by the electrons P_{abs} is written as follows [12-13]:

$$P_{abs} = \frac{nq^2 E_0^2}{2m_e} \frac{\nu_m}{\nu_m^2 + \omega^2} \tag{2.3}$$

where ω and υ_m is the angular frequency of VHF power source and electron collision frequency, respectively. Here q, m_e and E_0 is electron charge, electron mass and the amplitude of the electron oscillation in the VHF electric field. Although the plasma energy should be determined by solving the power balance equation, the mean power density calculated from Eq. (2.3) is considered to reflect the measured [(3/2) $n_e \kappa T_e$]. In this experiment, $\omega/2\pi$=60 MHz, $\nu_m/2\pi$~ 17 GHz at 1 Torr, that is, $\omega << \nu_m$, so that P_{abs} should decrease in proportional to ν_m^{-1} as shown in Eq. (2.4).

$$P_{abs} = \frac{nq^2 E_0^2}{2m_e \nu_m} \tag{2.4}$$

2.4 Power feeding

In the most experiments, a coaxial cable is used to feed VHF power to the power electrode of the parallel plate electrodes, so called conventional power feeding method. In the conventional power feeding method, one electrode is connected to the power supply through the matching box (M.B.), and another electrode is connected to the ground as shown in the Fig. 2.5. This type of a power feeding system has been applied in many studies. However, abnormal discharges happen between the power feeding cable and the chamber wall in the VHF range. To avoid such abnormal discharges, Nishimiya [14] has developed a new power feeding method, so called balanced power

feeding (BPF) method. As shown in Fig. 2.6, a balanced power feeding method is to use a power divider with the output of 180°, which providing two parallel Leher wires that are commercially used for TV antenna. This method shows how to feed VHF powers to the electrode by the balanced power feeding method.

Figure 2.7 and Figure 2.8 show the images of the VHF argon plasma by a conventional power feeding method and a balanced power feeding method, respectively. As seen in Fig. 2.7, the plasma is produced not only between the electrodes but also the area around the right wall. On the other hand, the plasma is mainly produced in the region between the two electrodes when we use the balanced power feeding method. This performance is explaining obviously of the advantage of the balanced power feeding method.

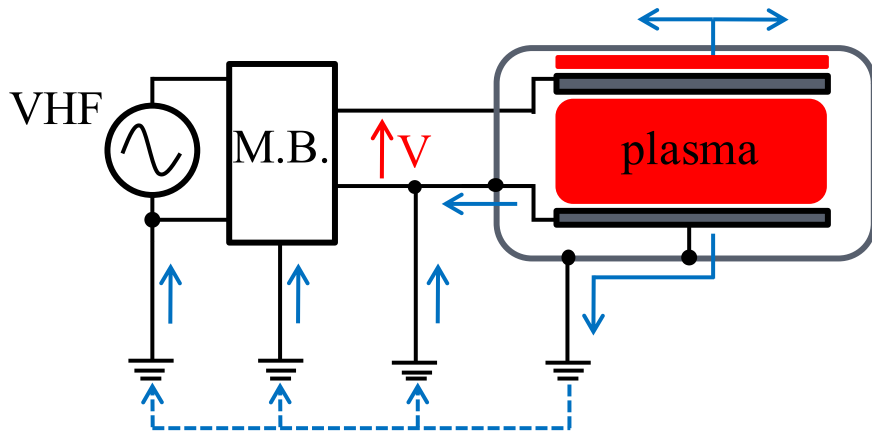

Fig. 2.5 Schematic of the conventional power feeding method.

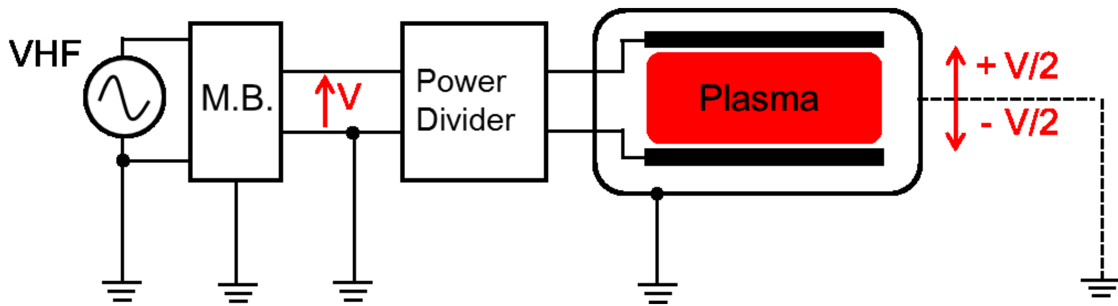

Fig. 2.6 Schematic of the BPF method.

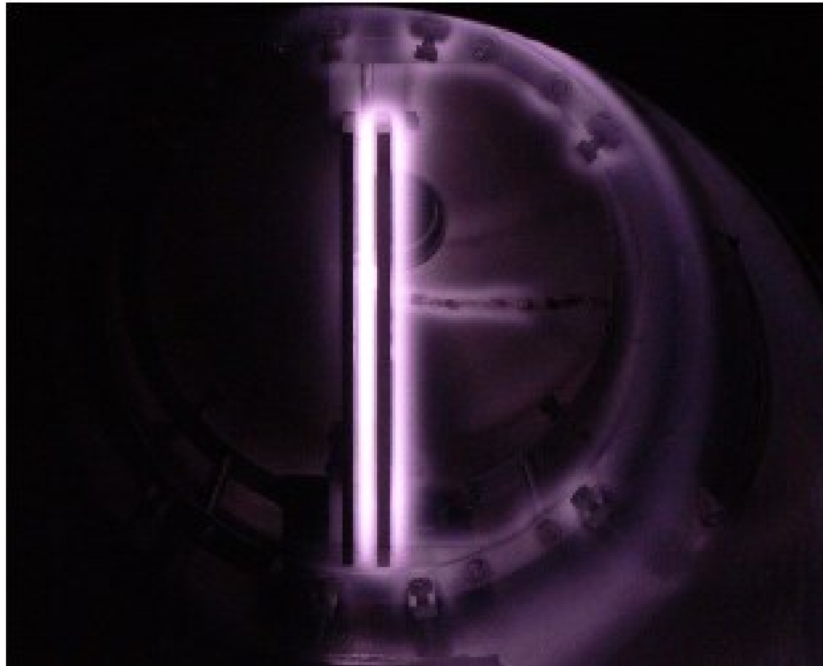

Fig. 2.7 Image of the VHF argon plasma by the conventional power feeding method.

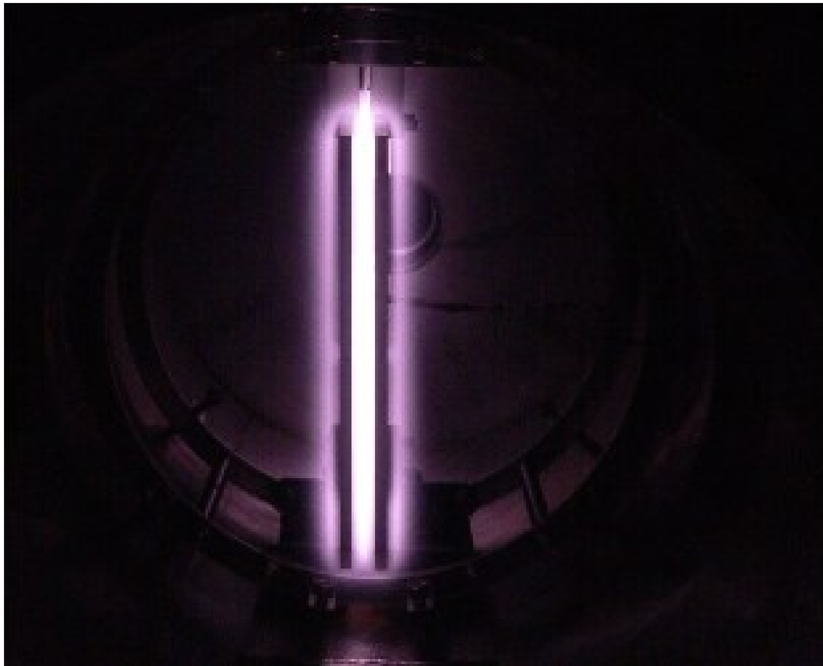

Fig. 2.8 Image of the VHF argon plasma by the balanced power feeding method.

2.5 Laser scattering

2.5.1 Laser Thomson scattering

LTS is the scattering of electromagnetic radiation by free charge particles. When an electromagnetic wave is incident on a charged particle, the electric and magnetic components of the wave exert a Lorentz force on the particle, setting it into motion. Since the wave is periodic in time, so is the motion of the particle. Thus, the particle is accelerated and consequently emits electromagnetic radiation. More exactly, energy is absorbed from the incident wave by the particle and re-emitted as an electromagnetic radiation.

If we consider a linearly polarized, monochromatic, plane wave incident on a particle carrying a charge q, the electric component of the wave is written as

$$\vec{\mathrm{E}} = \vec{\mathrm{e}}\mathrm{E}_0 e^{i(\vec{k}\cdot\vec{r}-\omega t)} \tag{2.5}$$

where E_0 is the peak amplitude of the electric field, $\vec{e}$ is the polarization vector, and $\vec{k}$ is the wave vector (of course, $\vec{e}\cdot\vec{\mathrm{k}} = 0$). The particle is assumed to undergo small amplitude oscillations about an equilibrium position which coincides with the origin of the coordinate system. Furthermore, the particle's velocity is assumed to remain sub-relativistic, which enables us to neglect the magnetic component of the Lorentz force. The equation of motion of the charged particle is given as

$$\vec{f'} = q\vec{E} = m\vec{S} \tag{2.6}$$

where m is the mass of the particle. $\vec{S}$ is its displacement from the origin. A charged particle that is accelerated radiates energy. When the particle velocity v is much smaller than the speed of light c, the radiated energy per unit time I_a^S is given by

$$I_a^S = \frac{q^2}{6\pi\varepsilon_0 c^3} v^2 \tag{2.7}$$

This type of radiation from a charged particle is called Thomson scattering.

The electron acceleration occurs in the direction of the electric field of the incident radiation, and so the scattered light has a characteristic direction of polarization. The relationship between the incident and scattered waves is shown in Fig. 2.9, for the case of linearly polarized incident light. The angle between the incident wavevector k_i, and the detected scattered wavevector k_s, is called a scattering angle and denoted by θ. The differential cross section for Thomson scattering $\sigma(\lambda_i, \theta)$ is independent of the wavelength of the incident light λ_i. The value of $\sigma(\lambda_i, \theta)$ for incident radiation with polarization direction φ is given by

$$\sigma(\theta) = r_0^2\left(1 - sin^2\theta cos^2(\varphi)\right) \tag{2.8}$$

In this expression, r_0 is the classical electron radius, given by

$$r_0 = \frac{e^2}{4\pi\varepsilon_0 m_e c^2} = 2.82 \times 10^{-15} m \tag{2.9}$$

The distribution of scattered radiation has an apple-shape, as shown in Fig. 2.9. One point to note is that there is no radiation in the direction of E_i.

For the case when the incident radiation is polarized, the cross section can be obtained by integrating Eq. (2.8) over φ and becomes

$$\sigma(\theta) = \frac{r_0^2(1+cos^2\theta)}{2} \tag{2.10}$$

The total Thomson scattering cross section σ_{Th} is given by

$$\sigma_{Th} = \int \sigma(\theta) d\Omega = \frac{8}{3}\pi r_0^2 = 6.65 \times 10^{-29}\ m^2 \tag{2.11}$$

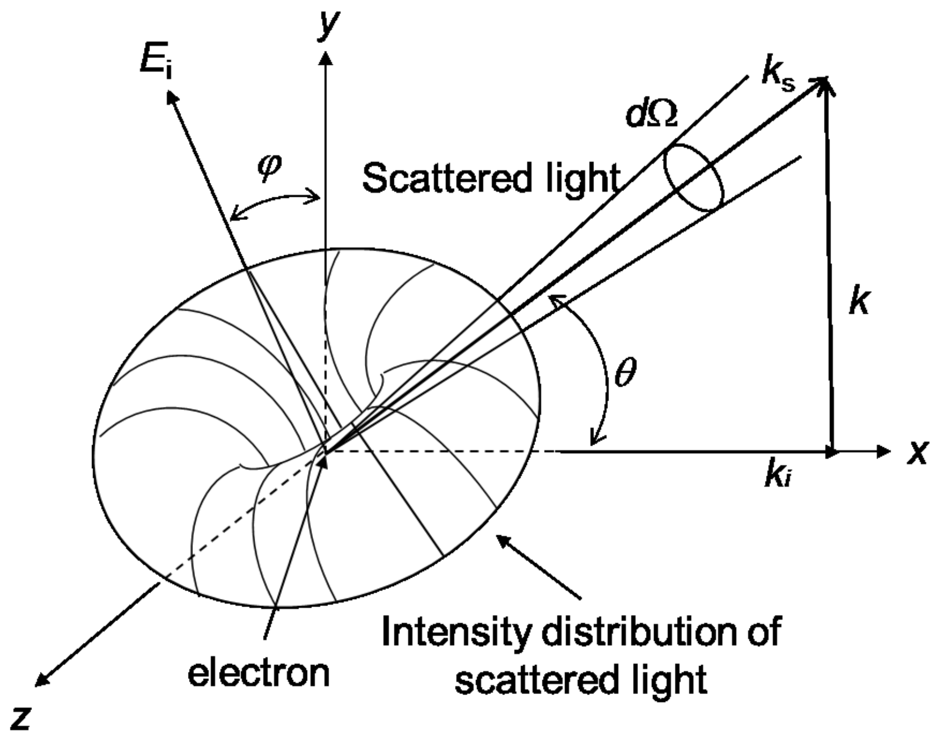

Fig. 2.9 The directional distribution of the Thomson scattered light intensity for the case of linearly polarized incident light with an electric field E_i.

As describe above, we consider the interaction of an electromagnetic wave with a plasma when the laser incident to the plasma. The wavelength of the scattered radiation reaches the detector is Doppler-shifted because the radiating charge is moving rapidly regarding to both the laser and the detector. The wavelength of the Doppler-shifted scattered light will be a function of the velocity component of the charge along the differential scattering wave vector, k, which is defined as the vector difference between the wave vector of the scattered light, k_s, and the wave vector of the incident laser beams, k_i, as shown in Fig. 2.9.

In the non-relativistic case, the velocity of the scattered particle can be assumed that the scattered radiation has approximately the same wavelength as the incident radiation and the absolute k value can be expressed as follow

$$|k| = |k_s - k_i| = 2|k_i| \sin\left(\frac{\theta}{2}\right) = \frac{4\pi}{\lambda_i} \sin\left(\frac{\theta}{2}\right) \tag{2.12}$$

The differential scattering wave vector and the Debye length, λ_D, are the two important parameters govern the shape of the Thomson scattering spectrum, as given by the scattering parameter, α, is expressed as follows

$$\alpha = \frac{1}{|k|\lambda_D} = \frac{\lambda_i}{\sin\left(\frac{\theta}{2}\right)} \left\{\frac{n_e e^2}{4\pi k_B T_e}\right\}^{\frac{1}{2}} \tag{2.13}$$

where λ_i is the wavelength of the incident laser radiation. Eq. (2.13) indicates α is affected by the laser wavelength, the electron temperature, the electron density, and the scattering angle. If the scattering is occurring over a distance that is smaller than the Debye length ($\alpha \ll 1$), the wave affects individual charges independently, producing incoherent scattering. Conversely, if the wavelength associated with the scattering wave vector k is comparable to or greater than the Debye length, so that $\alpha > 1$, the incident wave interacts with the shielded charges, causing them to undergo group motion and

producing called coherent scattering. Two scattering regions produce very different spectra, so the value of α in a particular experiment should be considered when the data are interpreted. In this study, our experimental condition meets incoherent scattering.

When Thomson scattering is in the incoherent scattering condition, the wavelength of the Doppler-shifted scattered light will be a function of the velocity component of the charge. The frequency of the scattered light, ω_s, may differ from the frequency of the incident light because of two subsequent Doppler shifts by the scattering particle. If the particle moves at a velocity, v, the wavelength of the laser light, λ, the incident light is scattered. The resulting frequency shift of the scattered waves us written as

$$\Delta\omega = \omega_s - \omega_i = k \cdot v \tag{2.14}$$

The Doppler shift of the scattered radiation, $\Delta\lambda$, is expressed as follows

$$\Delta\lambda = 2\mathrm{v} \sin\left(\frac{2}{\theta}\right) \cdot \frac{\lambda_i}{c} \tag{2.15}$$

For a Maxwellian EEDF, the electron velocity distribution function is given by

$$\mathrm{f}(v)dv = \left(\frac{m_e}{2\pi k_B T_e}\right)^{\frac{1}{2}} \exp\left(-\frac{m_e v^2}{2k_B T_e}\right) dv \tag{2.16}$$

By using Eq. (2.15) and Eq. (2.16), the dynamic form factor for Maxwellian EEDF can written as

$$\mathrm{S}(\Delta\lambda, \theta) d(\Delta\lambda) = \left(\frac{m_e}{2\pi k_B T_e}\right)^{\frac{1}{2}} \left(\frac{c}{2\lambda_i \sin\left(\frac{\theta}{2}\right)}\right) \exp\left\{-\frac{m_e v^2}{2k_B T_e}\left(\frac{c\Delta\lambda}{2\lambda_i \sin\left(\frac{\theta}{2}\right)}\right)^2\right\} d(\Delta\lambda) \tag{2.17}$$

Define the half width of the spectrum

$$\Delta\lambda_{Th} = \frac{2\lambda_i \sin\left(\frac{\theta}{2}\right)}{c} \sqrt{\frac{2k_B T_e ln2}{m_e}} \tag{2.18}$$

Using Eq. (2.18) yields Eq. (2.17) to be

$$\mathrm{S}^*(\Delta\lambda, \theta) d(\Delta\lambda) = \left(\frac{\ln 2}{\pi}\right)^{\frac{1}{2}} \frac{1}{\Delta\lambda_{Th}} \exp\left\{-\ln 2\left(\frac{\Delta\lambda}{\Delta\lambda_{Th}}\right)^2\right\} d(\Delta\lambda) \tag{2.19}$$

From Eq. (2.19), the Thomson scattered spectrum is Gaussian in shape if the EEDF is Maxwellian. $\Delta\lambda_{Th}$ is the half width at half maximum of the Gaussian spectrum and the electron temperature related to the width is given by

$$T_e = \frac{c^2 m_e}{8k_B \ln 2\left[sin^2\left(\frac{\theta}{2}\right)\right]}\left(\frac{\Delta\lambda_{Th}}{\lambda_i}\right) \tag{2.20}$$

The total Thomson scattering intensity is directly proportional to the electron density. Therefore, n_e can be determined from the measured spectrum if the absolute sensitivity of the detection system is accurately calibrated. In practice, this calibration is easily done by measuring the Rayleigh scattered intensity when the discharge chamber is filled with gas without a plasma. In the situation, the scattered signal intensities I_p (electron density from a plasma) and I_g (electron density from a known gas) are given by

$$I_P = n_e \sigma_T \Delta\lambda_P f_s \tag{2.21}$$

$$I_g = n_0 \sigma_R \Delta\lambda_g f_s \tag{2.22}$$

where σ_T and σ_R are the differential cross sections of the Thomson scattering and Rayleigh scattering, respectively. $\Delta\lambda_p$ and $\Delta\lambda_g$ are the spectral width of the scattered spectra from the plasma and the gas, and f_s is a function of the laser energy and efficiency of the detection system. The electron density is given by

$$n_e = n_0 \frac{I_P \sigma_R \Delta\lambda_g}{I_g \sigma_T \Delta\lambda_P} \tag{2.23}$$

The spectral widths of the measured spectra are convolutions of the true scattered spectra and the instrument function of the spectrometer used to measure the spectra. However, the actual Rayleigh width is extremely small; the width of the measured gas spectrum is simply the width of the instrument function of the spectrometer.

2.5.2 Rayleigh scattering

The scattered spectrum which is measured from a plasma usually contains a Rayleigh scattered component, as well as the Thomson scattered component. Rayleigh scattering occurs by scattering of the laser light by electrons bound in neutral and ionic particles. When the density of neutral particles is much larger than that of ions, which is generally the case for glow discharge plasmas, a measurement of the Rayleigh scattered signal yields the density of neutral panicles in the discharge. The measurement system has to be calibrated, but this is already necessary for the Thomson scattering measurement and so does not involve an additional measurement.

2.5.3 Stray light

This is the radiation from the laser source that reaches the detector by different ways rather than scattering from the plasmas. In practice, the Thomson signal is overlapped by both the Rayleigh scattering signal and the stray light signal. Because the Thomson scattering cross section is very small, it is very important to minimize this stray light, in order to be able to measure Thomson spectra.

The stray light is conveniently expressed in terms of the pressure of gas that gives a comparable signal level due to Rayleigh scattering. The knowledge of the ratio of the Thomson to Rayleigh cross sections permits the stray light level to be expressed in terms of the number density of free electrons that would give a scattered light signal of the same intensity. This ratio is

$$\frac{\sigma_e}{\sigma_R} = \left(\frac{e^4}{m_e^2 c^2}\right)\left(\frac{\lambda^4}{4\pi^2}\right)\frac{N^2}{(n-1)^2} \tag{2.24}$$

where N is the number density of molecules and n is the refractive index of the gas at a pressure of 1 atom, and λ is the wavelength of the light undergoing scattering.

The windows through which the laser beam enters and leaves the plasma vessel

scatter more light than the plasma itself. It is therefore important that these windows be invisible from the detectors. To achieve this, the windows are mounted at the ends of entrance and exit tubes furnished with suitable stops and baffles. After the exit window, a light dump is arranged whose purpose is to absorb the laser beam once it has traversed the plasma. To avoid seeing stray light that undergoes several unpredictable reflections and scatterings on the walls of the plasma vessel, it is desirable that the detector should look into a black hole. For that purpose, a viewing dump, consisting of a blackened cone, is placed inside the vacuum system in a port opposite the detection window, as shown in Fig. 2.10.

The remaining stray light is discriminated from Thomson scattering by the dispersing element of the detecting system, because the stray light as well as Rayleigh scattering are distinguished from scattered by the fact that the latter two are concentrated at the laser wavelength, whereas the scattered light is Doppler-broadened.

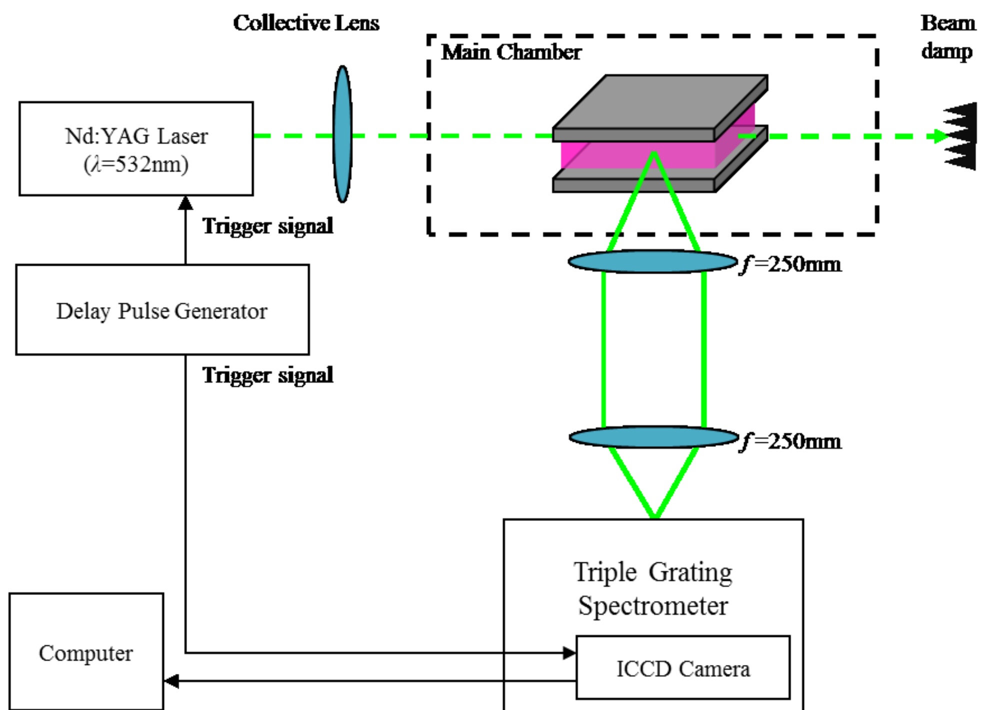

Fig. 2.10 Schematic diagram of the laser Thomson scattering system.

2.5.4 Experimental setup of LTS system

A schematic diagram of the LTS system is shown in Fig. 2.10. The main chamber (diameter 200 mm, length 400 mm) was specifically designed for LTS measurements. The chamber was equipped with baffles, two Brewster windows, a beam dump, and a triple grating spectrometer (TGS). This TGS made it possible to detect the Thomson scattering spectrum at 1 nm away from the laser wavelength without the problem of stray light. Finally, the scattered light signals passing through the TGS were detected by an ICCD camera (Princeton Instruments, PI-MAX III). The quantum efficiency of the camera was ~50 % at $\lambda = 532$ nm. The photon counting method was applied to enable reliable measurements of small scattered signals.

As mentioned previously, the LTS technique was first applied to high temperature, high density fusion plasma ($n_e > 10^{19}$ m^{-3}). For this kind of plasmas, one laser shot is usually used to get Thomson scattering spectrum because the number of Thomson scattered photons is large enough and there no contribution from Rayleigh scattering. If the same technique is used in lower density glow discharge plasma, such as electron cyclotron resonance (ECR) discharge, inductively coupled resonance plasma (ICP) discharge, and capacitive coupled plasma (CCP) discharge, there is a limit to the number of Thomson scattered photons which can be detected beside the presence of Rayleigh scattered photons. This limitation can be overcome some extent by accumulating data for a large number of laser shots. If this technique is applied to low density plasma ($n_e \sim 10^{15}$ m^{-3}), which is applied in this study, then Thomson scattering spectrum could not be separated from Rayleigh scattering spectrum and stray light.

The main difficulties of designing an LTS system for low density plasmas are a small intensity of detected Thomson signals and the small separation of the scattered

spectra from a Rayleigh signal and a stray light signal.

Regarding the first difficulty of small scattered signals, the total number of photoelectrons N_{pe} is given by

$$N_{pe} = \left(\frac{E_L}{h\nu}\right) n_e \Delta L \sigma_T(\theta)\, \eta \Delta \Omega \qquad (2.25)$$

where E_L is the laser intensity, h is the Planck's constant, ν is the laser frequency, n_e is the electron density, ΔL is the scattering volume, σ_T is the Thomson scattering cross section, η is the transmission of the detection system, and $\Delta\Omega$ is the detection solid angle. If the second harmonic of a YAG laser (wavelength of 532 nm, laser energy of 300 mJ, repetition rate of 10Hz, and pulse duration of 10ns) is used and $E_L/h\nu = 8.1 \times 10^{17}$ photons, ΔL = 10 mm, $\sigma_T = 8 \times 10^{-30}$ m^2/sr, η is around 0.17 due to the transmission of the gratings and lenses, $\Delta\Omega$ = 0.08 sr (focal lens of 250 mm, diameter of 80 mm), we get $N_{pe} = 8.8 \times 10^{-16}\, n_e$, which is a small number. For example, N_{pe} = 0.2 p-e for a plasma having electron density $n_e = 10^{15}$ m^{-3}.

In order to overcome the difficulty of the small LTS photons, an accumulation of the measured data for a large number of laser pulses and the using of a photon counting system are indispensable. Also, a careful design of the detection optics is required, together with increasing the scattering volume and the detection solid angle.

To overcome the other difficulty problem of the stray light, Brewster windows, the baffles, a beam dump, a viewing dump, and a triple grating spectrometer (TGS) are used.

A special TGS which was equipped with a notch filter for eliminating Rayleigh scattering and stray light, and thereby providing a dispersed LTS spectrum with Rayleigh and stray light highly suppressed. The TGS contains a narrowed entrance slit, three gratings, mirrors, and lenses. The first imaging element illuminates the grating by

the incident light and second imaging element is used to focus the dispersed light to the exit plane. Due to the non-idealities of the optics and the finite width of the entrance slit, the relationship between the spatial position in the exit plane and wavelength is not sharp. If a perfectly monochromatic light illuminates the entrance slit of a spectrometer, the spectrum is recorded in the exit plane has a certain width. The shape of this spectrum is called instrumental function of the spectrometer, and its half width at half maximum (HWHM) is called the instrumental half width.

Figure 2.11 shows a schematic diagram of the TGS. It was mainly composed of three Shimazu holographic grating (Grating 1, 2, and 3) (60mm × 60mm with 1200 groves /mm, and blazed at 500 nm) and they were adjusted so that their center wavelength is 532 nm. Six anti-reflection-coated achromatic doublet lenses (Lens 1-6) having high transmission of about 99.4%, were used as imaging elements. Lens 1, Lens 3, and Lens 5 were used to illuminate Grating 1, Grating 2, and Grating 3 with collimated parallel light, respectively. On the other hand, Lens 2, Lens 4, and Lens 6 were used to focus the light onto the Notch filter, the central slit (Slit 2), and the photo-cathode of the ICCD camera, respectively.

The grooves of the grating are perpendicular to the plane of the paper shown in Fig. 2.12. The light strikes the grating at an incident angle, i to the grating normal, θ is the diffracted angle. When defining integer m as the diffraction order and d as groove spacing, maximum constructive interference is found to occur under the condition

$$d(\sin i \pm \cos \theta) = m\lambda \tag{2.26}$$

From Eq. (2.26), it is obvious that if parallel rays carrying multiple wavelength components fall on the grating, each wavelength within the same order will have a distinctive value of θ determined by the grating equation. Consequently, a

polychromatic light is spatially dispersed. The dispersion of a grating spectrometer determines its ability to separate wavelengths. The inverse linear dispersion of a spectrometer can be found by calculating the change in wavelength λ with respect to change in distance x along its focal plane.

$$\frac{\Delta\lambda}{\Delta x} = \frac{d\cos\theta}{fm} \tag{2.27}$$

where d, θ, and f are the grating groove spacing, diffraction angle, and effective system focal length, respectively.

In the spectrometer used in this study, the grating constant m = 1200 groves/mm, focal length of the first lens (Lens 1), and angles of incidence and reflection of the grating 1 are 5° and 35°, respectively. The focal length of lens 2 is 250 mm, which yields, combined with the mentioned parameters, an inverse dispersion of 2.7 nm/mm from the first grating 1. The light within $\Delta\lambda = \pm$ 0.68 nm from the laser wavelength was blocked since the width of the Rayleigh block was 0.5 mm.

From Fig. 2.11, it can be seen that Grating 1 dispersed the incident light (Stray light, Rayleigh scattering, plasma emission, and Thomson scattering) and Lens 2 focused the dispersed spectrum onto the notch filter (0.5 mm wide vertical strip) which in turn blocked the central part of the spectrum (stray light and Rayleigh scattering). Grating 2 recombined the rest of the spectrum (Plasma emission and Thomson scattering), which was then focused by Lens 4 onto Slit 2. Combining above optic elements with the third parts (Grating 3, Lens 5, and Lens 6) yielded dispersion of the Thomson scattering signal with a high rejection for detection by ICCD camera (Princeton Instruments, PI-MAX III).

The notch filter width determined the rejection factor; a broader width results in a higher rejection with a wider profile. Therefore, the width must be at least the same

width with the entrance slit (Slit 1). The stray light originated from the gratings where it scattered the Rayleigh light when it dispersed or recombined the incident light. The scattered light was suppressed by Slit 2. The instrumental half width ($\Delta\lambda_{Ih}$) of the TGS depends on the entrance slit width, the focal length of Lens 5 and Lens 6, and the inverse dispersion (R nm/mm) of Grating 3, where

$$\Delta\lambda_{Ih} = \frac{1}{4} S \times \frac{f_6}{f_5} \times R \tag{2.28}$$

The TGS in this thesis is designed specific for the LTS system for measuring VHF argon plasmas, where the electron density is estimated to the order of 10^{16} m^{-3}.

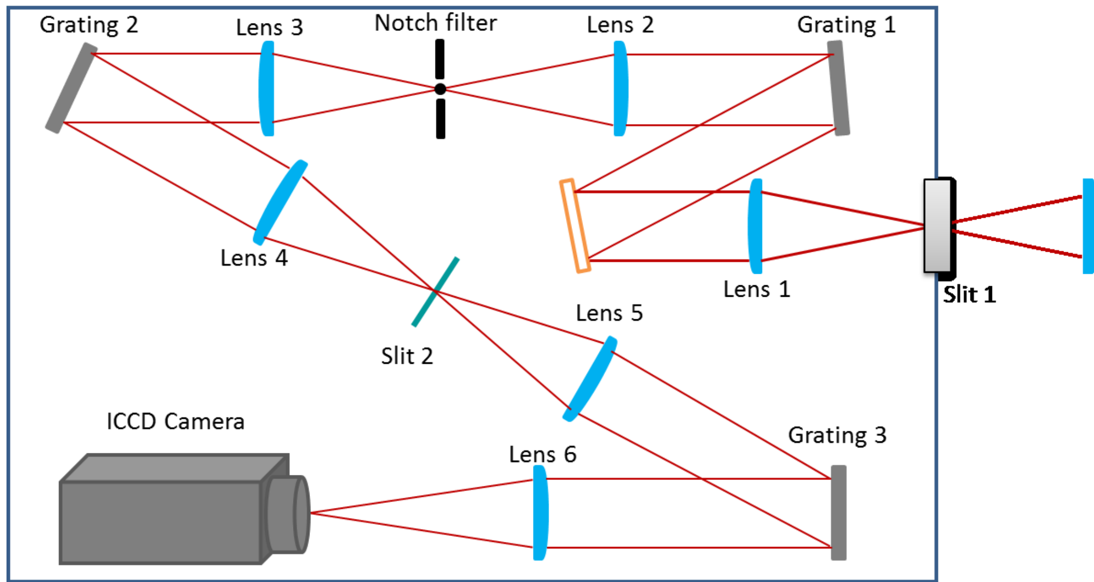

Fig. 2.11 Schematic diagram of TGS.

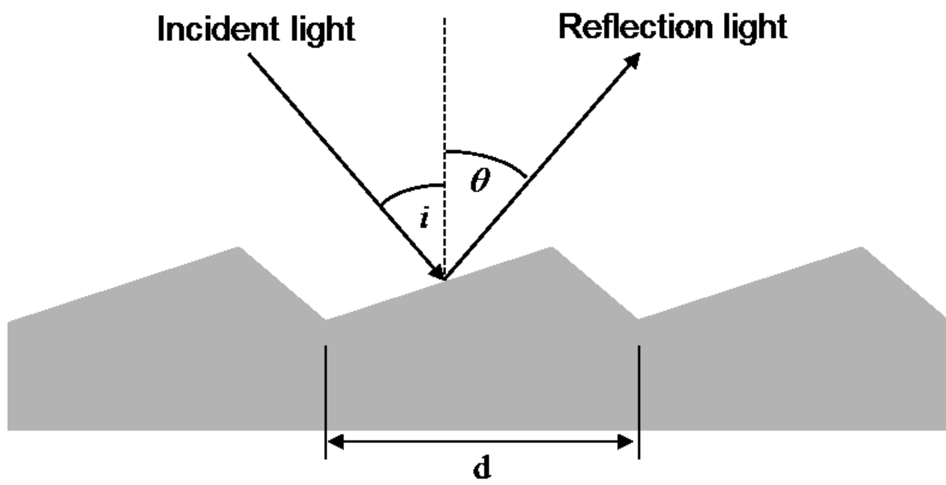

Fig. 2.12 Reflections from the grating surface.

2.6 Langmuir probe method

The Langmuir probe is the simplest method to measure the plasma parameters. The most extensive use of the Langmuir probe is in the industry such as silicon thin film solar cells and semiconductors, where non-thermal plasmas are used for deposition and etching. Recently there is a tendency to produce plasma at high pressures to obtain high rates of deposition and etching. These partially ionized plasmas require special techniques in probe construction and theory.

2.6.1 Characterization of the probe [15]

When the potential applied to the probe V_p is much larger than the space potential V_s ($V_p >> V_s$), an electron current I_e is collected. Here, the probe current is negative. When $V_p << V_s$, an ion current I_i is collected. *I-V* curves are plotted as shown in Fig. 2.13.

As shown in Fig. 2.13, it can be divided into three main parts; ion saturation region (part III), transition region (part II), and electron saturation region (part I). The space potential (V_s) is near the bended point of the curve. At the part III (ion saturation region), where all the electrons are repelled, the ion saturation current (I_{sat}) is obtained. The Floating Potential (V_f), is where the ion and electron currents are equal, and the net current is zero. In the part II, the ion current is negligible, and the electrons are partially repelled by the negative potential $V_p - V_s$. In a Maxwellian plasma, the current increases exponentially in this part. When V_p reaches V_s, all of the electrons is collected. In the part I, I_e grows only slowly because of the expansion of the sheath. From *I - V* curve, the electron density n_e, electron temperature T_e, and plasma potential V_s can be determined.

Figure 2.14 shows a typical I-V curve measured in this experiment. Argon gas was used here and the gas pressure and the VHF power were 100 mTorr and 20 W,

respectively. The dc bias voltage is varied from -80 V to +80 V while the DC current flowing to the probe measured. From Fig. 2.14, it can obtain much information what we introduced in above. From those, the plasma parameters, such as T_e and n_e can be estimated. The detailed procedure for calculating T_e and n_e are explained in the next paragraph.

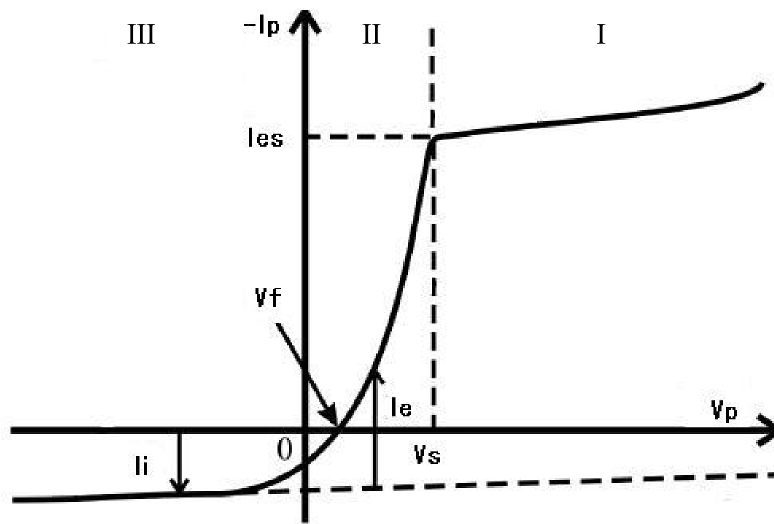

Fig. 2.13 Schematic of the I-V curve obtained by the probe method.

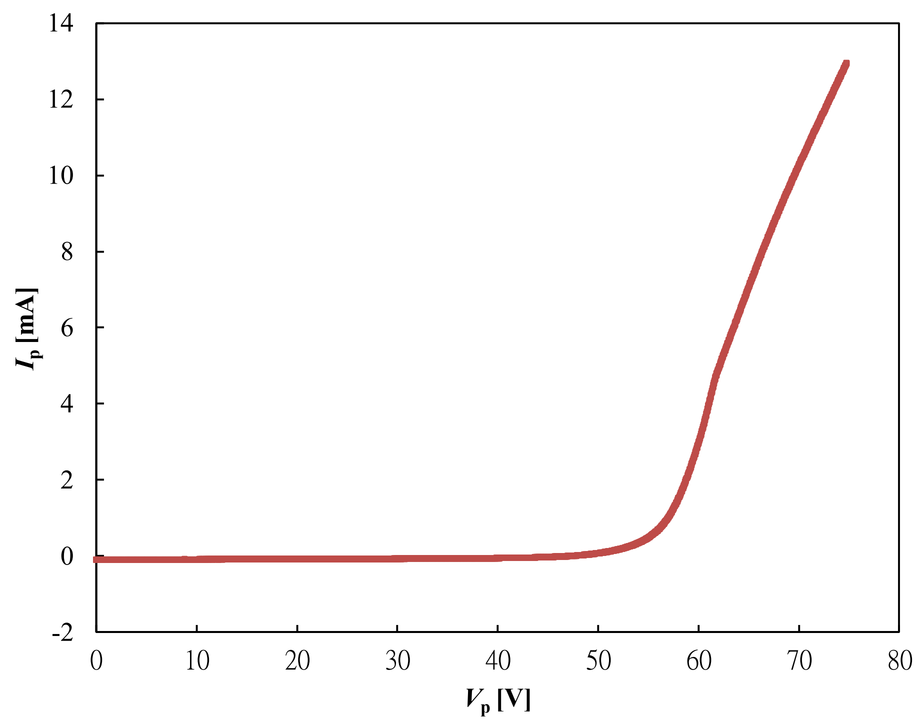

Fig. 2.14 A typical I-V curve measured in this experiment.

I. Transition region

When the *I-V* curve is plotted semi-logarithmically, the exponential part should be a straight line if the electrons have a Maxwellian velocity distribution function:

$$I_e = I_{es} exp\left[e\left(V_p - V_s\right)/k_B T_e\right] \tag{2.29}$$

where

$$I_{es} = \frac{1}{4} e\, S\, n_e \overline{V} = e\, S\, n_e \left(\frac{k_B T_e}{2\pi m}\right)^{\frac{1}{2}} \tag{2.30}$$

where S being the surface area of the probe tip, k_B is the Boltzmann constant, and m is the ion mass. Here, I_{es} is the electron saturation current, or thermal current to a surface at V_s. Eq. (2.29) shows that the slope of the (ln I) − V_p curve is exactly $1/T_e$ and is a good measure of the electron temperature. We can obtain the electron temperature by the equation as follows.

$$\frac{d \ln\left|I_e\right|}{dV} = -\frac{e}{k_B T_e} \tag{2.31}$$

II. Ion saturation region

In the part III on the probe curve of Fig. 2.13, the potential is sufficiently negative with respect to the plasma potential that only ions are collected by the probe. This is ion saturation current, and the total current is

$$I_{is} = \frac{1}{4} e S n_i \overline{v_i} \tag{2.32}$$

where S is the area of the probe, n_i is the ion density, and v_i is the mean thermal velocity of ions that leave the plasma. Substituting the ion thermal velocity into Eq. (2.32) yields

$$I_{is} = \frac{1}{4} e\, S\, n_i \sqrt{\frac{8 k_B T_i'}{\pi M}} \tag{2.33}$$

where T_i is the ion temperature in *K*, and *M* the ion mass.

As well known, ions do not have a Maxwell distribution. Thus, in order to obtain the ion saturation current, we have to solve the sheath equation derived from the Poisson equation. According to the sheath theory [16], the ion saturation current is expressed by

$$I_{is} = \alpha_P e n_0 S \sqrt{\frac{k_B T_e}{m_i}} \qquad (2.34)$$

Setting Eq. (2.29) and Eq. (2.34) equal yields

$$V_f = V_s - \frac{k_B T_e}{2e} \ln\left(\frac{2M}{\pi m}\right) \qquad (2.35)$$

The potential difference (V_s-V_f) is called the wall potential that corresponds to the ion bombardment energy. The theoretical value is $\alpha_p = \exp(-1/2) = 0.61$. We can estimate the electron density obtained from the ion saturation current by Eq. (2.36).

$$n_i[\mathrm{m}^{-3}] = n_e[\mathrm{m}^{-3}] = 2.56 \times 10^{17} \times \frac{I_{is}[\mathrm{mA}]\sqrt{m_i}[\mathrm{kg}]}{S[\mathrm{cm}^2]\sqrt{T_e}[\mathrm{eV}]} \qquad (2.36)$$

III. Electron saturation region

Since the probe in electron saturation collects all electrons incident on the plasma-sheath boundary, the total electron current collected by the probe is given as

$$I = I_e = \frac{1}{4} e n_e S \overline{v_e} = \frac{1}{4} e n_e S \left(\frac{8 k_B T_e}{\pi m_e}\right)^{\frac{1}{2}} = I_{es} \qquad (2.37)$$

Where S is the surface area of the probe, n_e is the electron density, v_e is the mean thermal velocity of the electrons, and m_e is the electron mass.

From Eq. (2.37), the electron density can be estimated from the electron saturation current.

$$n_e = \frac{I_{es}}{eS}\left(\frac{2\pi m_e}{k_B T_e}\right)^{\frac{1}{2}} \qquad (2.38)$$

Thus, we can estimate the electron density from the ion saturation current, Eq. (2.36), and the electron saturation current, Eq. (2.38). Theoretically, both should be the same. However, in the presence of magnetic fields and negative ions, the electron saturation current becomes lower than theoretical value, so that Eq. (2.36) is widely used to estimate the electron density. In this experiment, we estimated the electron density using Eq. (2.36).

2.6.2 Construction of the probe

Usually, the probe tip is made of a tungsten rod or wire having a diameter in the range 0.1−1 mm. The rod is insulated by a ceramic tube from the plasma except for a short length of exposed tip, about 10 mm long. These probe tips can be exposed to low-temperature plasmas without melting. To avoid disturbing the plasma, the ceramic tube should be as thin as possible, preferably < 1 mm in diameter. The assembly is encased in a vacuum jacket, which could be a stainless steel or glass tube 1/4″ in outside diameter. It is preferable to make the vacuum seal at the outside end of the probe assembly rather than at the end immersed in the plasma, which can cause a leak. Ideally, only the ceramic part of the housing should be allowed to enter the plasma. For this study, the area of the probe wire was 9.5×10^{-6} m^2 (the diameter of the tungsten is 0.3 mm, the length is 10 mm). The structure of the experimental setup and the probe tip assembly is shown in Fig. 2.15 and Fig. 2.16, respectively.

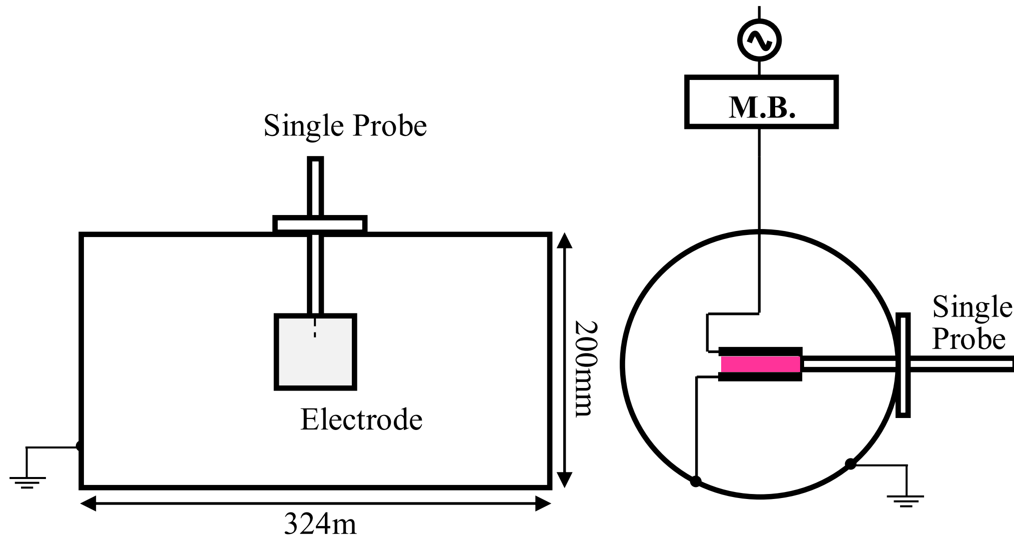

Fig. 2.15 Top view and side view of the experimental setup.

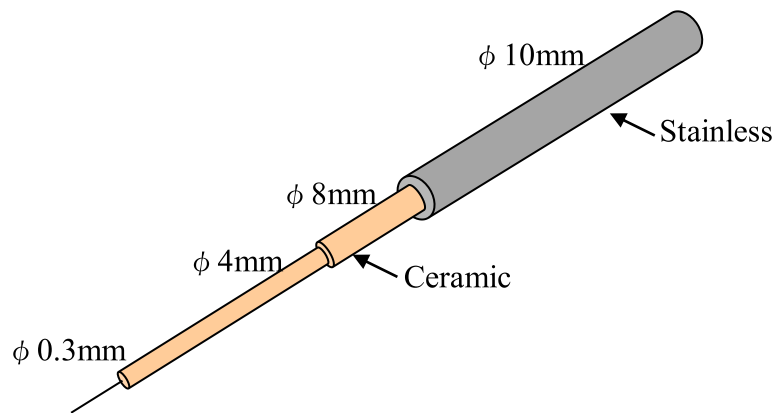

Fig. 2.16 Schematic diagram of the probe.

2.7 Simulation

The production of a VHF discharge plasma with large area at high pressure is one of the key technologies in the fabrication of thin-film silicon solar cells because the VHF discharge plasma provides the high-rate film deposition with a low electron temperature [17]. However, in this type of discharge, as already described, anomalous discharges occur outside the discharge electrodes. The anomalous discharges consume a large amount of the input power and cause unstable discharges inside the electrodes. Moreover, the anomalous discharges damage components around them, for example a power feeding cable, as the result, the film is contaminated with the sputtered materials. Thus, the occurrence of the anomalous discharges must be avoided for large area and qualified solar cells. As one of the techniques to avoid the occurrence of the anomalous discharges, a balanced power feeding (BPF) method has been proposed [14]. Nishimiya et al. [14] demonstrated that this method successfully suppresses anomalous discharges and the electron density is higher than that without BPF.

We have studied the VHF plasma produced by the BPF method for effective application to the PECVD. In our previous work [18], we calculated the VHF hydrogen plasma produced by the BPF method, in which we focused on the effects of the VHF voltages applied to each electrode with same amplitude and opposite signs. We confirmed that the BPF method improved the VHF hydrogen plasma characteristics with short-gap parallel plate electrodes: the electron density outside the electrodes significantly decreased and the electron density and the absorbed power increased inside the electrodes compared to those in the conventional single-electrode power feeding (SPF) model. Thus, the advantage of the BPF method was shown in this preliminary work. In this study, we examined the characteristics of a VHF argon plasma produced by

the BPF in detail.

2.7.1 Description of the model

The simulation of a VHF plasma produced by the BPF method was performed by using the Plasma Hybrid Module (PHM) of PEGASUS software Inc. [19]. The PHM has been developed on the basis of the Hybrid Plasma Equipment Model formed by Kushner and his colleagues [20]. The detailed description of the PHM is described in our previous paper [18]. Here, we briefly outline the computational procedure of the PHM. The density and the temperature of electrons, which are utilized for the calculation of the electron energy distribution functions (EEDFs) by Monte Carlo method, are calculated by the fluid model and the equation of the electron motion. The density and the velocity of ions are determined by solving the equations of continuity in which the drift diffusion model is applied to the particle fluxes. For neutral particles, Navier-Stokes equation and the advective diffusion equation are derived. Some CCP models, which were demonstrated by Lymberopoulos and Economou [21] and by Rauf and Kushner [22], were calculated by using the PHM, and the simulation results of PHM showed good agreements in the previous researches.

The BPF model we used here is a cylindrical coordinate system with axial symmetry, as shown in Fig 2.17. A pair of parallel disk electrodes, whose radius is 34 mm, is situated in the center of a cylindrical chamber. The gap between the electrodes is fixed to 8 mm. The outside surfaces of the electrodes are covered with insulators, in order to suppress the emission of electric energy from them. In the BPF model, two VHF voltages V_{top} and V_{bottom}, whose amplitudes and phases are equal to and opposite from each other, are applied to the top and the bottom electrodes, respectively:

$$V_t = V_{rf}\sin(2\pi f t) + V_{dc,t} \ , \ V_b = V_{rf}\sin(2\pi f t) + V_{dc,b} \qquad (2.39)$$

Here, V_{rf} and f are the amplitude and the frequency of the applied voltages, respectively. In this paper, f is fixed to 60 MHz. Self-bias voltages of each electrode $V_{dc,\,t}$ and $V_{dc,\,b}$ are included in the equations. The input power P_{elec} is defined as a time-averaged integral of the products of the applied voltages and the currents flow to the electrodes:

$$P_{\mathrm{elec}} = P_{\mathrm{t}} + P_{\mathrm{b}} = \frac{1}{T_{\mathrm{rf}}}\int_0^{T_{\mathrm{rf}}} \left(V_{\mathrm{t}} I_{\mathrm{t}}(t) + V_{\mathrm{b}} I_{\mathrm{b}}(t)\right) dt \tag{2.40}$$

Here, T_{rf} is the time of a VHF cycle, and I_t and I_b are currents flow to the top and the bottom electrodes, respectively. The input power P_{elec} is equivalent to the total power absorbed in the calculating volume.

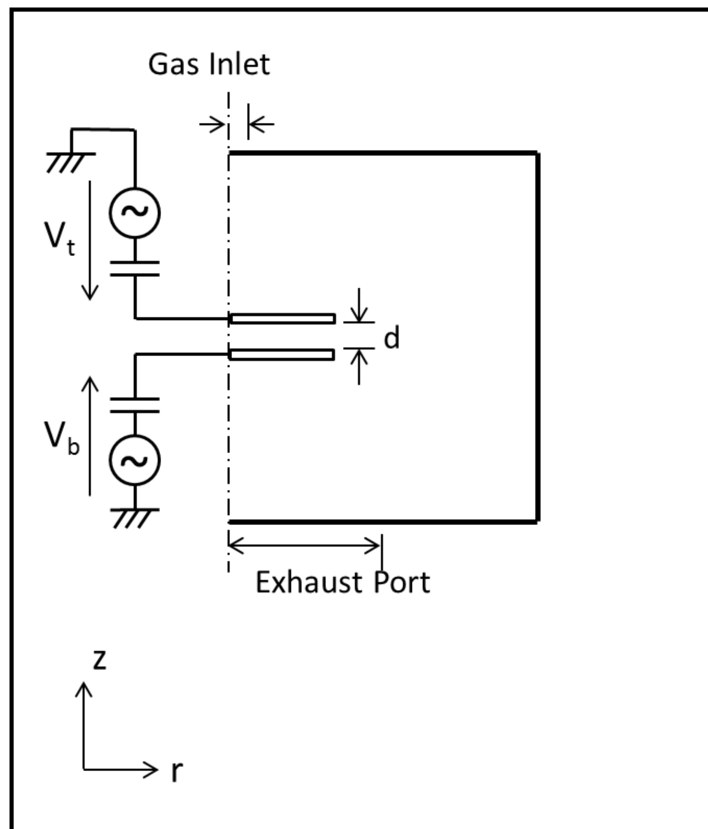

Fig. 2.17 Schematic diagram of BPF model.

References

[1] H. F. Sterling and R. C. G. Swann, Solid-State Electron, vol. 8 (1965) pp. 653-654.

[2] R. C. Chittick, J. H. Alexander and H. F. Sterling, J. Electrochem. Soc., vol. 116 (1969) pp. 77-81.

[3] A. J. Lewis, J. G. A. N. Connel, W. Paul, J. R. Pawlik and R. J. Temkin, in Tetrahedrally Bonded Amorphous Semiconductors, eds. M. H. Brodsky, S. Kirkpatrck, and D. Weaire, AIP Conf. Proc., vol. 20 (1974) p. 27.

[4] A. Triska, D. Dennison and H. Fritzsche, Phys. Soc., vol. 20 (1975) p.392.

[5] F. Meilland et al. in 31th IEEE Photovoltaic Specialist Conference Lake Buena Vista, FL, USA. (2005).

[6] A. Shah, J. Meier, A. Buechel, U. Kroll, J. Steinhauser, F. Meillaud, H. Schade, D. Domine, Thin Solid Films 502 (2006) 292–299.

[7] A. Shah, J. Meier, E. Vallat-Sauvain, C. Droz, U. Kroll, N. Wyrsch, J. Guillet, U. Graf, Thin Solid Films 403 –404 (2002) 179–187.

[8] Jatindra K. Rath, Yanchao Liu, Monica Brinza, Arjan Verkerk, Caspar van Bommel, A. Borreman, Ruud E.I. Schropp, Thin Solid Films 517 (2009) 4758-4761.

[9] G. Neuman, U. Banziger, M. Kammeyer, and M. Lange, Rev. Sci. Instrum., 64 (1993) 19.

[10] Lawrence J. Overzet, and Michael B. Hopkins, J Appl. Phys., 74 (1993) 4323.

[11] Ch Lukas, M. Muller, V. Schulz-von der Gathen, and H. F. Dobele, Plasma Sources Sci. Technol., 8 (1999) 94.

[12] S. C. Brown, *Introduction* to *Electrical Discharges* in *Gases*, Chap.10 (John Wiley & Sons, 1966).

[13] M. A. Lieberman and A. J. Lichtenberg, *Principles of Plasma Discharges and Materials Processing*, Chap.4 (John Wiley & Sons, 1994).

[14] T. Nishimiya, Y. Takeuchi, Y. Yamauchi, H. Takatsuka, T. Shioya, H. Muta, Y. Kawai, Thin Solid Films **516**, 4430, (2008).

[15] Francis F. Chen, Mini-Course on Plasma Diagnostics, IEEE-ICOPS meeting, Jeju, Korea (2003).

[16] Francis F. Chen, John D. Evans, and Donald Arnush, Phys. Plasmas, Vol. 9, No. 4, April 2002.

[17] M. Kondo, M. Fukawa, L. Guo and A. Matsuda, 2000 J. Non-Cryst. Solids **266-269,** 84.

[18] K. Ogiwara, W. Chen, K. Uchino and Y. Kawai, to be published in Thin Solid Films.

[19] PEGASUS Software Inc., http://www.psinc.co.jp/english/index.html.

[20] M. J. Kushner, 2009 J. Phys. D: Appl. Phys. **42** 194013.

[21] D. P. Lymberopoulos and D. J. Economou, 1995 J. Res. Natl. Inst. Stand. Technol. **100** 473.

[22] S. Rauf and M. J. Kushner, 1997 J. Appl. Phys. **82** 2805.

Chapter 3

Diagnostics of VHF Argon Plasmas by Laser Thomson Scattering

3.1 Introduction

Very-high-frequency (VHF) plasmas are widely used to fabricate microcrystalline silicon thin-film solar cells [1-2]. However, the deposition rate of microcrystalline silicon is much lower than that required by industry. A high-pressure depletion method [3-4] in which the VHF plasma is produced with a narrow discharge gap at high pressures was proposed recently to increase the deposition rate. However, faster deposition of microcrystalline silicon is needed to reduce the production cost of solar cells. The deposition rate is closely related to plasma characteristics. Thus, an important subject in the study of microcrystalline silicon thin-film solar cells is the measurement of the parameters of the VHF plasma produced by a narrow gap discharge.

There are several methods to measure plasma properties. The Langmuir probe method can be used to investigate the characteristics of VHF plasmas, such as the electron density n_e and the electron temperature T_e. However, the parameters of a plasma produced by a narrow gap discharge will be seriously disturbed when the probe is inserted. In addition, the probe cannot be used at gas pressures higher than 10 Torr, because the ion mean-free path is much shorter than the sheath length, and ion collisions frequently occur in the sheath [5].

The laser Thomson scattering (LTS) method is a powerful diagnostic method under such conditions. Therefore, we have been applying LTS to various discharge plasmas.

When LTS is applied to VHF plasmas, a high power-laser light source is required to secure an adequate signal-to-noise ratio of the Thomson scattering signal, because the electron densities of VHF plasmas are expected to be relatively low ($<10^{17}$ m^{-3}). We must also consider the laser disturbance of the plasma. We used argon gas at pressures ranging from 0.1 to 1 Torr as the working gas, and the second harmonic (wavelength 532 nm) of a YAG laser as the light source. Under these conditions, metastable argon atoms in the plasma may be photo-ionized by two-photon absorption of laser photons. Yamamoto [6] recently reported that the Thomson scattering signal was affected by the photo-ionization of metastable xenon atoms when LTS experiments were performed with laser power densities of $> 10^{15}$ W/m^2. In this study, we examined the influence of the photo-ionization of metastable argon atoms on the Thomson scattering spectrum and the laser power density at which the photo-ionization becomes a problem for the LTS diagnostics of argon plasmas.

3.2 Experimental setup

Figure 3.1 and Figure 3.2 show a schematic of the LTS system for the VHF plasma. The chamber (diameter 200 mm, length 400 mm) was specifically designed for LTS measurements. The chamber was equipped with baffles, two Brewster windows, a beam dump, and a triple grating spectrometer (TGS). The structure and function of the TGS have been reported in Ref. [7]. This TGS made it possible to detect the Thomson scattering spectrum at 1 nm away from the laser wavelength without the problem of stray light. Finally, the scattered light signals passing through the TGS were detected by an ICCD camera (Princeton Instruments, PI-MAX III). The quantum efficiency of the camera was ~50 % at λ= 532 nm. The photon counting method was applied to enable reliable measurements of small scattered signals.

The 60-MHz VHF plasma was sustained between two parallel-plate electrodes (60 mm × 60 mm × 8 mm) made of stainless steel; the distance between them was always maintained at 10 mm. The working gas was argon; the gas pressures used in this study were 500 mTorr and 100 mTorr, and the VHF power ranged from 20 W to 80 W. In the conventional power feeding method, one electrode is connected to the power supply through the matching box, and another electrode is connected to the ground. This type of a power feeding system has been applied in many studies. However, abnormal discharges can be produced between the power feeding cable and the chamber wall in the VHF range. To avoid such abnormal discharges, we used a balanced power feeding method [8]. Thus, the plasma was mainly produced in the region between the two electrodes.

To examine the effect of the photo-ionization of metastable argon atoms, Thomson scattering experiments were performed under two conditions with greatly different laser power densities by using a plano-convex lens and a cylindrical lens as the focusing lens of the probing laser beam as shown in Fig. 3.3. Both lenses had focal lengths of 500 mm, and the probing laser energy was 300 mJ. When the plano-convex lens was used, the diameter of the laser spot at the measuring point was 160 μm (full width at half-maximum). The estimated laser power density for this case was 1.5×10^{15} W/m^2. When the cylindrical lens was used, the laser spot seen from the detection optics side was 290 μm in height and 8 mm in depth. The laser power density in this case was 1.3×10^{13} W/m^2. For these experiments, plasmas were produced at an argon gas pressure of 500 mTorr and a VHF power of 80 W.

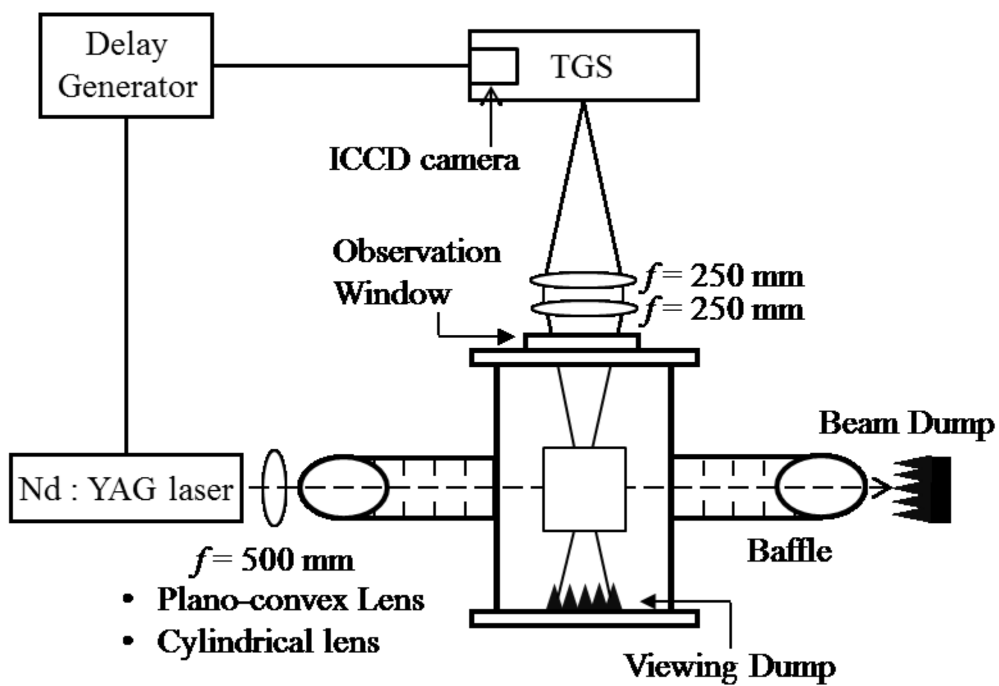

Fig. 3.1 Schematic diagram of experimental setup (top view).

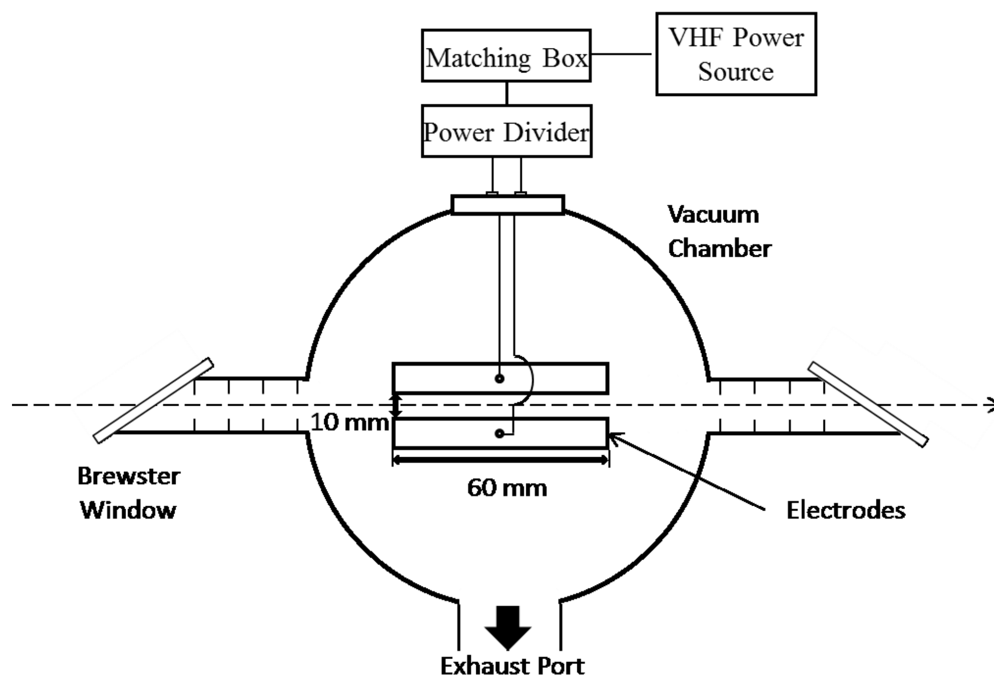

Fig. 3.2 Schematic diagram of experimental setup (side view).

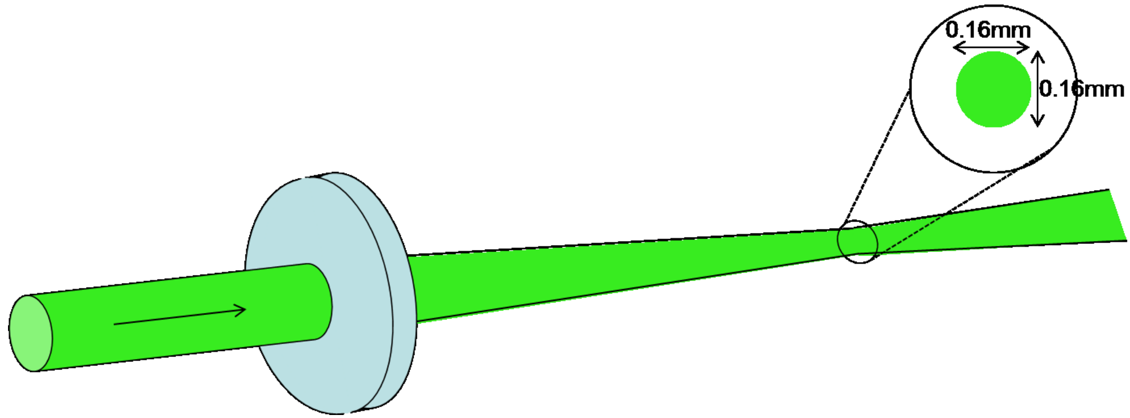

(a) Plano-convex lens

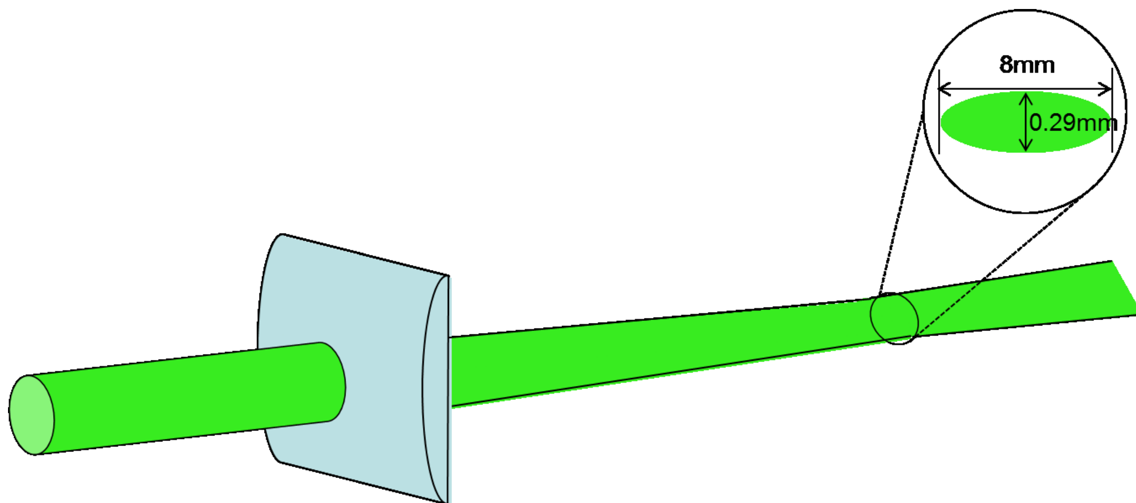

(b) Cylindrical lens

Fig. 3.3 Schematic diagrams of (a) the plano-convex lens and (b) the cylindrical lens.

3.3 Results and discussion

The experimental results are shown in Fig. 3.4, which compares the spectra observed using the cylindrical and plano-convex lenses. Each data point represents signals accumulated over 40,000 laser shots. As noted above, the signals were detected by the ICCD camera. The 29 plotted data points are in the wavelength range from $\Delta\lambda$ = 1.204 nm to $\Delta\lambda$ = 3.612 nm with an interval of 0.086 nm. Here $\Delta\lambda$ is the wavelength difference between the laser wavelength and the measured wavelength.

The ordinate is the detected photon number on a logarithmic scale; the abscissa is $(\Delta\lambda)^2$. In this plot, a straight line indicates a Gaussian spectrum, and therefore a Maxwellian electron energy distribution function. As can be seen from Fig. 3.4, the data points for the cylindrical lens case fall on a single line. The line gives an electron density of $n_e = 1.6 \times 10^{17}$ m^{-3} and an electron temperature of T_e = 3.1 eV.

On the other hand, for the plano-convex lens case, the spectrum was fitted by two lines. The gradient of the line with the moderate slope agrees well with that of the line fitted for the cylindrical lens case. When the steeper spectrum is subtracted from the moderate slope spectrum, the resultant spectrum gives an electron temperature of 0.5 eV, assuming a Gaussian spectrum. Thus, the average energy of this low-energy component is around 0.75 eV.

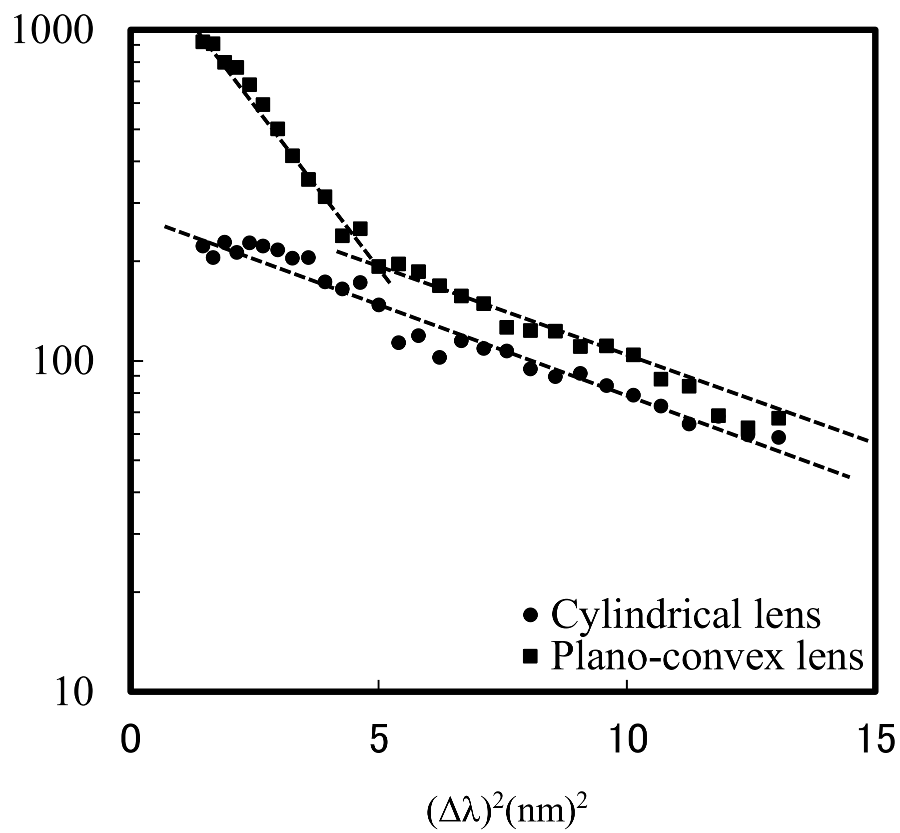

Fig. 3.4 Thomson scattering spectra obtained using the plano-convex and cylindrical lenses.

Metastable argon atoms have two energy levels: 11.55 eV and 11.72 eV [9]. The energy obtained by two-photon absorption of the probing laser light should be 4.66 eV. On the other hand, the energies required to ionize argon to the metastable states are 4.22 eV and 4.03 eV. Therefore, the excess energies of 0.44 eV and 0.63 eV can be delivered to the free electrons that are released by two-photon ionization from the argon metastable states.

These facts show that the average energy of the low-energy component and the energies acquired by electrons produced by photo-ionization are comparable. In fact, the intensity of the low-energy component decreased when the probing laser energy was decreased. Therefore, it can be considered that the low-energy component was produced by the photo-electrons as a result of the photo-ionization of metastable argon atoms.

Then, we examined the dependence of the intensity of the low-energy component against the laser power density. The measurements were performed for various laser power densities. As a measure of the intensity of the low-energy component, signals in the wavelength range from $\Delta\lambda$=1.2 nm to $\Delta\lambda$=1.6 nm were integrated. The results are shown in Fig. 3.4. In this figure, both the signal count number (the ordinate) and the laser power density (the abscissa) are plotted on a logarithmic scale.

In Fig. 3.5, the solid line, which is the sum of a linear function (slope 1) and a cubic function (slope 3), is well fitted to the data points with laser power densities below 7×10^{13} W/m^2. Above this range (>10^{14} W/m^2), the signal intensity increases with a slope of 1.5 against the laser power density. This is interpreted as follows. At laser power densities below 1×10^{13} W/m^2, the signal is proportional to the laser power density, and the effect of the photo-ionization of metastable argon atoms is negligible. The critical laser power density at which the real Thomson scattering signal is

comparable to the effect of the photo-ionization of metastable argon atoms is around 4×10^{13} W/m^2. In the second range of laser power density, between 4×10^{13} W/m^2 and 7×10^{13} W/m^2, the effect of the photo-ionization of metastable argon atoms dominates. In this range, the signal is determined by the two-photon ionization process and the Thomson scattering (one-photon process), and therefore is proportional to the third power of the laser power density. In the third region, where the laser power density is greater than 7×10^{13} W/m^2, the signal is again almost linear with respect to the laser power density. This may be due to the depletion of metastable argon atoms, because most of them are ionized early in the strong laser pulse. However, the spatial profile of the laser power density has a tail to some extent; the signal increases with a slope of 1.5 against the laser power density.

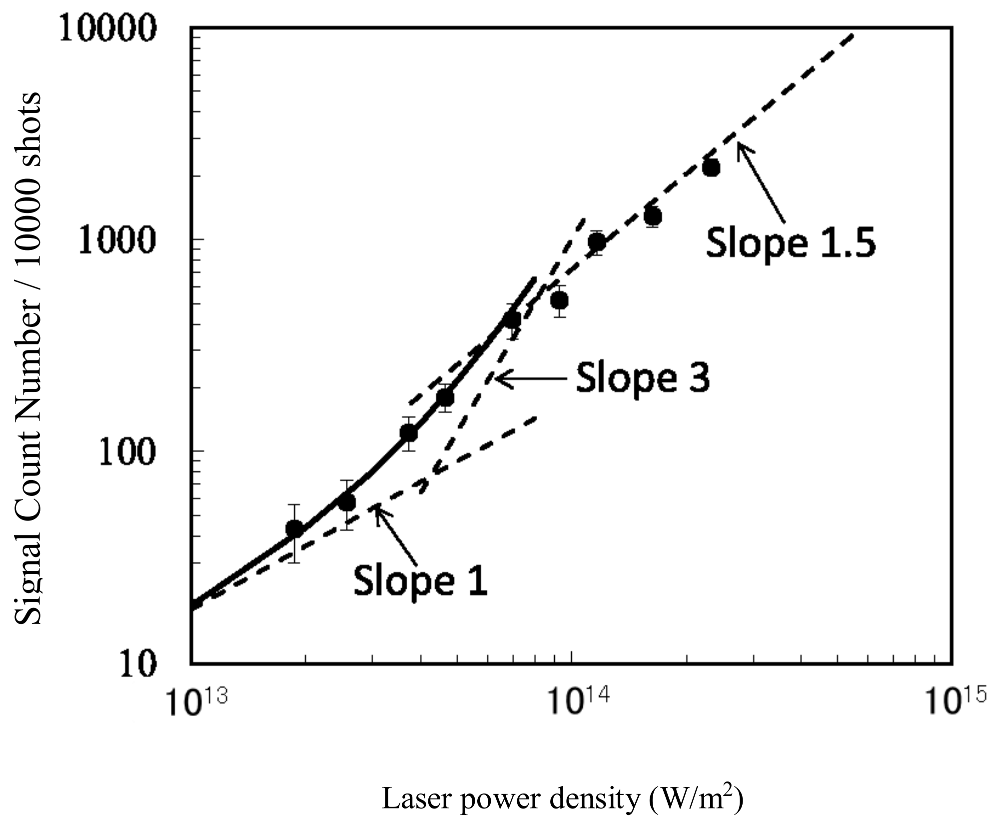

Laser power density (W/m^2)

Fig. 3.5 Dependence of signal count number on laser power density.

Now we know that LTS can be applied to VHF argon plasmas when the laser power density is below 1×10^{13} W/m^2. This power density can be easily realized by using a cylindrical lens as shown in Fig. 3.3 (b). Because the focal depth of the detection optics was around 2 mm, only 30 % of the scattered power can be detected by the detection optics. However, the use of the cylindrical lens as a focal lens is effective to keeping the signal level to be not so much different from that obtained by using a plano-convex lens as a focal lens.

We compared the values of the electron density and electron temperature measured by LTS using the cylindrical lens as the focusing lens and the Langmuir probe. We selected an argon gas pressure of 100 mTorr so that the ion mean-free path could be comparable to the sheath length, and the results of the probe might be relatively reliable.

The results are shown in Fig. 3.6 and Fig. 3.7. The electron density values obtained by LTS are about 10 % higher than those obtained by the probe, and the values of the electron temperature obtained by LTS are about 1.7 times lower than those obtained by the probe. This tendency is in agreement with previous reports [10-11]. Therefore, these results further support the validity of the results of LTS measurements.

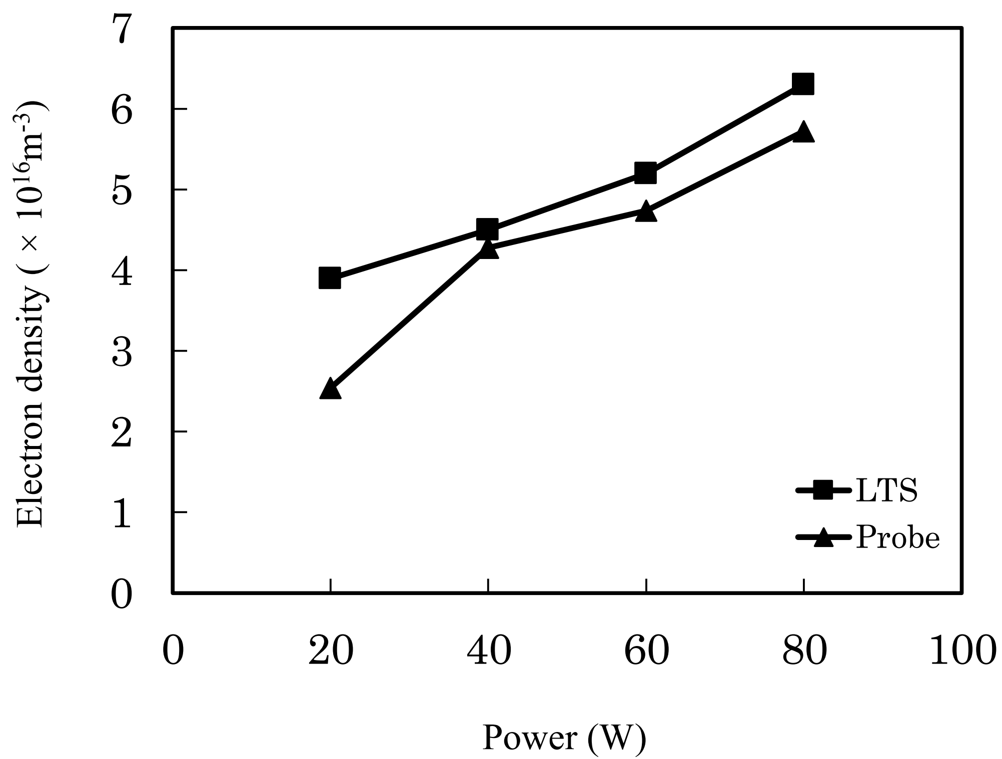

Fig. 3.6 Dependence of the electron density obtained by the LTS and Langmuir probe methods on the VHF power. Argon gas pressure was 100 mTorr.

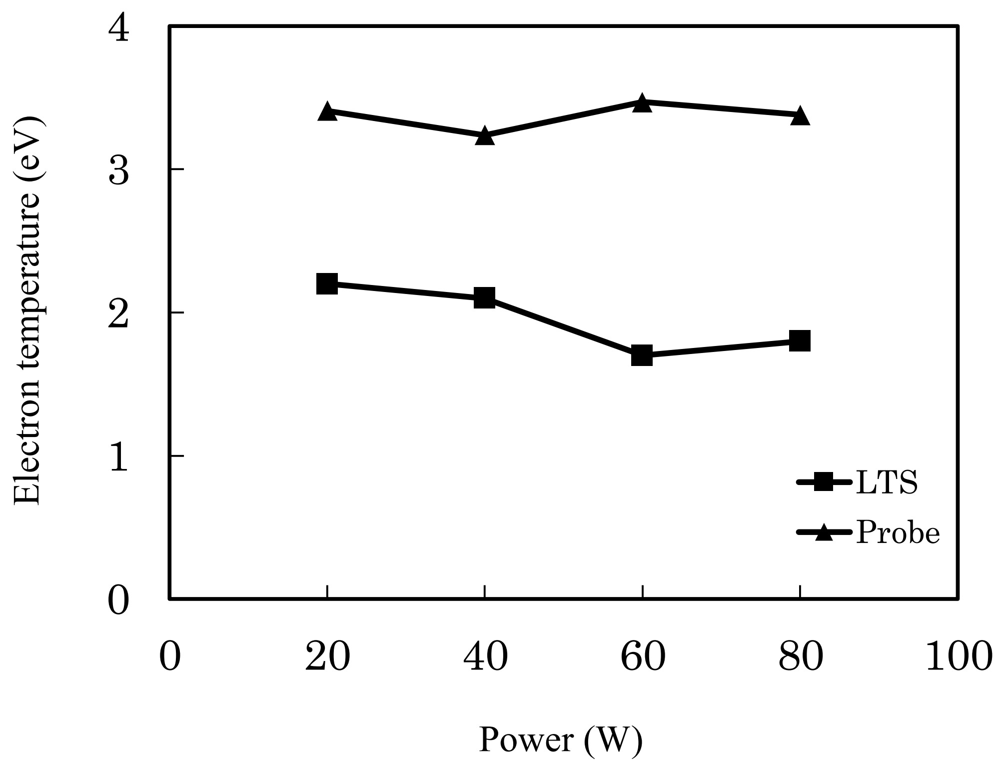

Fig. 3.7 Dependence of the electron temperature obtained by the LTS and Langmuir probe methods on the VHF power. Argon gas pressure was 100 mTorr.

3.4 Summary

In conclusion, we examined the applicability of LTS to the diagnostics of VHF argon plasmas. As a result, it was shown that the photo-ionization of metastable argon atoms affects the Thomson scattering spectrum when the probing laser power density is greater than 4×10^{13} W/m^2. The threshold laser power density may change slightly according to the ratio of the metastable argon density and the electron density. Unexpectedly, the threshold laser power density for argon gas was lower than that for xenon gas by a factor of 20.

We succeeded in removing the influence of the photo-ionization of metastable argon atoms on the Thomson scattering spectrum of the VHF argon plasma by reducing the power density of the YAG laser below 1×10^{13} W/m^2.

References

[1] Y. Yamauchi, Y. Takeuchi, H. Takatsuka, H. Yamashita, H. Muta and Y. Kawai, Contributions to Plasma Physics **48**, 4, 326 (2008).

[2] S. Y. Myong, K. Sriprapha, Y. Yashiki, S. Miyajima, A. Yamada and M. Konagai, Sol. Energy Mater. Sol. Cells **92**, 639 (2008).

[3] U. Graf, J. Meier, U. Kroll, J. Bailat, C. Droz, E. Vallat-Sauvain, A. Shah, Thin Solid Films **427**, 37 (2003).

[4] M. Isomura, M. Kondo and A. Matsuda, Jpn. J. Appl. Phys. **41**, 1947 (2002).

[5] T. E. Sheridan and J. Goree, Phys. Fluids B **3**, 4, 326 (2008).

[6] N. Yamamoto, K. Tomita, K. Sugita, T. Kurita, H. Nakashima, and K. Uchino, Rev. Sci. Instrum. **83**, 073106 (2012).

[7] S. Hassaballa, M. Yakushiji, Y. Kim, K. Tomita, K. Uchino, and K. Muraoka, IEEE Trans. Plasma Sci. **32**, 1 (2004).

[8] T. Nishimiya, Y. Takeuchi, Y. Yamauchi, H. Takatsuka, T. Shioya, H. Muta, Y. Kawai, Thin Solid Films **516**, 4430, (2008).

[9] NIST Atomic Spectra Database Levels Form, http://physics.nist.gov/PhysRefData/ASD/levels_form.html.

[10] M.D. Bowden, M. Kogano, Y. Suetome. T. Hori, K.Uchino, and K. Muraoka, J. Vac. Sci. Technol. A **17**, 493 (1999).

[11] M. Noguchi, T. Hirao, M. Shindo, K. Sakurauchi, Y. Yamagata, K. Uchino, Y. Kawai and K. Muraoka, Plasma Sources Sci. Technol. **12**, 403 (2003).

Chapter 4

Investigation of VHF Argon Plasma at High Pressure by Balanced Power Feeding

4.1 Introduction

A very high frequency (VHF) plasma is widely used for the fabrication of microcrystalline silicon thin film solar cells [1-2] because it provides high deposition rates. Recently the high pressure depletion method [3-4] has been proposed to increase the deposition rate. In this case, the VHF plasma is produced with the narrow discharge gap at high pressures. Now faster depositions of microcrystalline silicon are needed for further cost reduction of solar cells. The deposition rate is proprtional to the electron density, so that the production of a higher electron density plasma is required from industry.

A VHF plasma is characterized by electron trapping, that is, the electron displacement δx should be shorter than a spacing gap between discharge electrodes for $\omega << \upsilon_m$ [5]:

$$\delta x = \frac{qE_0}{m_e \omega v_m} << \frac{d}{2} \qquad (4.1)$$

Here d is a spacing gap between discharge electrodes, ω and υ_m is the angular frequency of VHF power source and electron collision frequency, respectively, and q, m_e and E_0 is electron charge, electron mass and the amplitude of the VHF electric field. Electron trapping effect provides better confinement of electrons and as a result the electron density becomes high. Eq. (4.1) indicates that E_0 and υ_m are important parameters in the

VHF plasma, that is, the VHF power and pressure are key parameters in the VHF plasma characteristics. When VHF powers are increased, the amplitude of the VHF electric field E_0 increases and as a result the condition for electron trapping, $\delta x << d/2$, is not valid. Therefore, to increase υ_m by increasing the pressure is required for VHF plasma discharge at high powers. Thus, it is an important subject in the production of microcrystalline silicon solar cells to examine the characteristics of the VHF plasma produced with a short gap discharge.

The Langmuir probe method is mostly used to investigate the characteristics of the VHF plasma such as the electron density (n_e) and the electron temperature (T_e). However, the plasma parameters with the narrow gap discharge will be seriously disturbed when the probe is inserted. In addition, the probe cannot be used at high pressure because the ion mean free path is much shorter than the sheath length, leading to the overestimation of the ion density [6].

In the previous paper [7], we examined how the photo-ionization of metastable argon atoms affects the Thomson scattering spectrum and at which laser power density the photo-ionization becomes a problem for the Laser Thomson scattering (LTS) diagnostics of argon plasmas. We succeeded in removing the influence of the photo-ionization of the metastable argon atoms on the Thomson scattering spectrum from the VHF argon plasma by reducing the power density of the YAG laser below 1×10^{13} W/m^2. Thus, we consider that the LTS can be a powerful diagnostic method under such conditions.

In this paper, we examined the dependence of the VHF plasma parameters on the pressure and power by using the LTS method, where a VHF plasma was produced by a balanced power feeding method [8] in addition to the conventional power feeding

method. In addition, we tried to simulate the VHF plasma using the Plasma Hybrid Module (PHM) of PEGASUS software.

4.2 Results and discussion

4.2.1 Comparison of conventional and balanced power feeding

In order to examine the effect of the conventional power feeding and balanced power feeding method on the plasma parameters, we measured n_e and T_e using the LTS system as a function of VHF power. As seen in Fig. 4.1 and Fig. 4.2, when the VHF power is increased from 20 watt to 80 watt, n_e increases from 3.9×10^{16} m^{-3} to 6.3×10^{16} m^{-3} for the case of balanced power feeding method. The n_e values obtained for the case of the balanced power feeding method were higher about 40 % than those obtained for the conventional power feeding method. Thus, we conclude that the balanced power feeding method provides higher electron density. On the other hand, as seen in Fig. 4.2, T_e tends to decrease with increasing the power independent of the power feeding method.

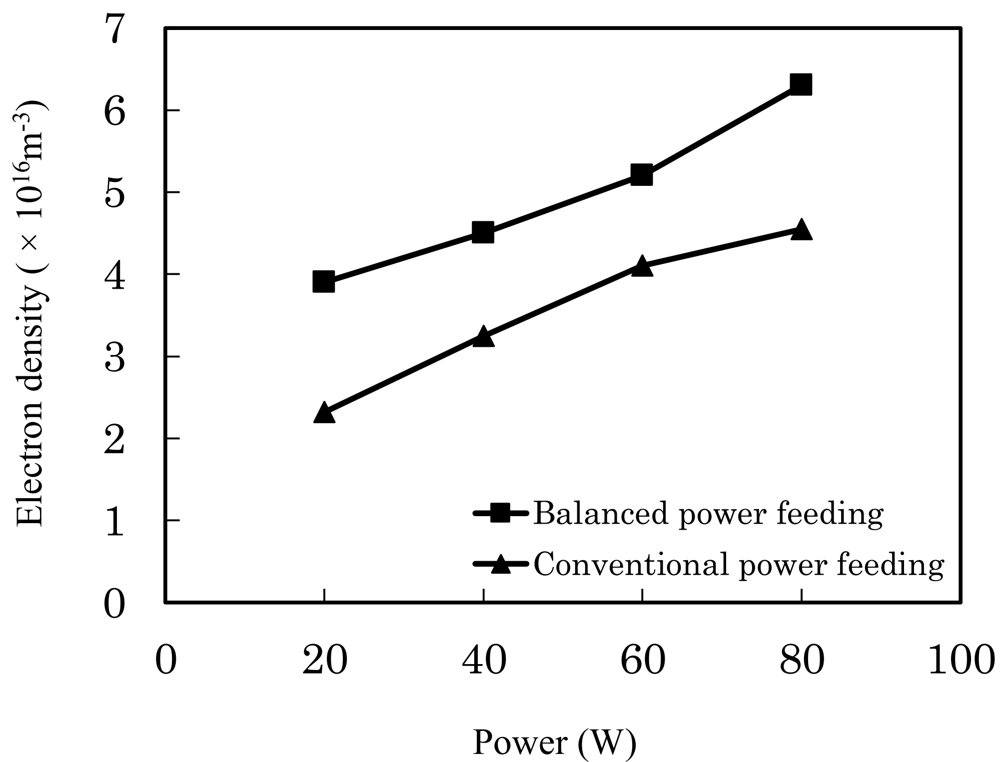

Fig. 4.1 Dependence of the electron density on the VHF power is compared for the case of the balanced power feeding method and the case of the conventional feeding method. Here the pressure was 100 mTorr.

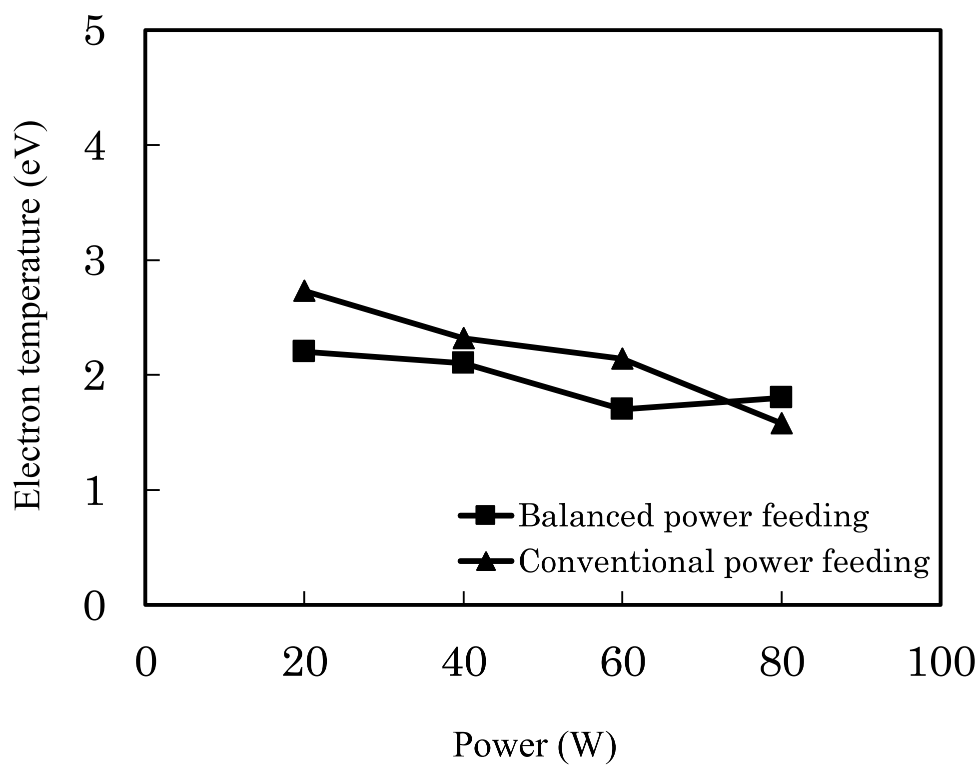

Fig. 4.2 Dependence of the electron temperature on the VHF power is compared for the case of the balanced power feeding method and the case of the conventional feeding method. Here the pressure was 100 mTorr.

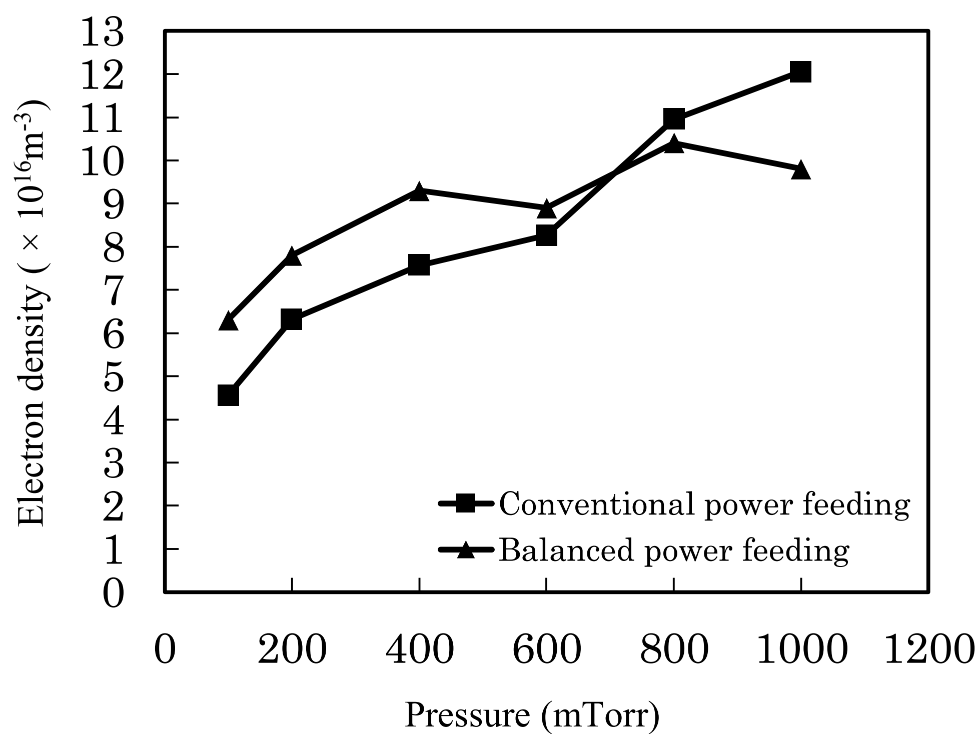

Fig. 4.3 Dependences of the electron density on the gas pressure is compared for the case of the balanced power feeding method and the case of the conventional feeding method. Here the VHF power was fixed at 80 W.

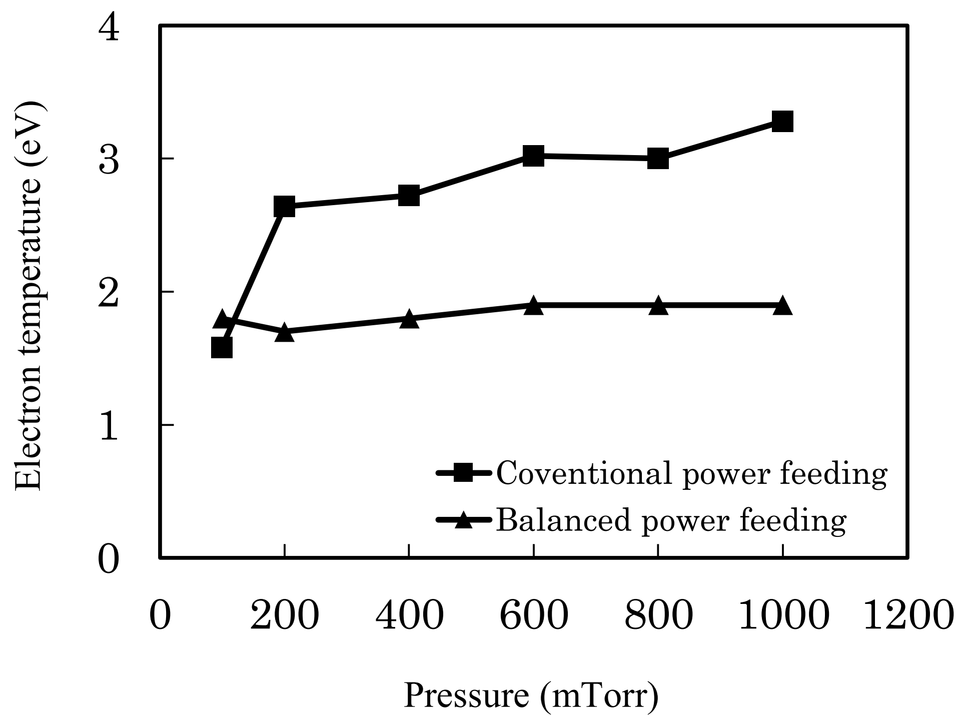

Fig. 4.4 Dependences of the electron temperature on the gas pressure is compared for the case of the balanced power feeding method and the case of the conventional feeding method. Here the VHF power was fixed at 80 W.

Then we measured the dependence of the plasma parameters on the gas pressure. Figure 4.3 shows that when the pressure is increased, the electron density increases. This is understood by electron trapping effect described in Sec. 2.3.1. Looking at carefully Fig. 4.3, the results can be divided into two parts in the case of using the balanced power feeding method. In the first part, n_e increases from 6.3×10^{16} m^{-3} to 1.0×10^{17} m^{-3} when the gas pressure is increased from 100 mTorr to 800 mTorr. In the second part, when the gas pressure is increased from 800 mTorr to 1000 mTorr, n_e is saturated at 1.0×10^{17} m^{-3}. On the other hand, n_e increases from 4.6×10^{16} m^{-3} to 1.2×10^{17} m^{-3} when the conventional power feeding method is used. The average n_e ratio of the balanced power feeding method is 20 % lower than that by the conventional power feeding method when the gas pressure is higher than 800 mTorr. This may be caused by the abnormal discharges which were observed near the power feeding point on the side of the powered electrode for the case of the conventional power feeding with gas pressures > 200 mTorr. As described in Sec. 2, Eq. (2.4) suggests that when the pressure is increased, the electron density decreases at high pressures, so that the electron density in this case will decrease for the pressure higher than 1 Torr.

Figure 4.4 shows that T_e is always kept around 1.8 eV independent of the pressure when the balanced power feeing method is used. In the case of the conventional power feeding method, T_e is around 3.0 eV except at 100 mTorr, this maybe also caused by the abnormal discharges. Note that the balanced power feeding method provides lower electron temperature plasma that is favorable for plasma processes.

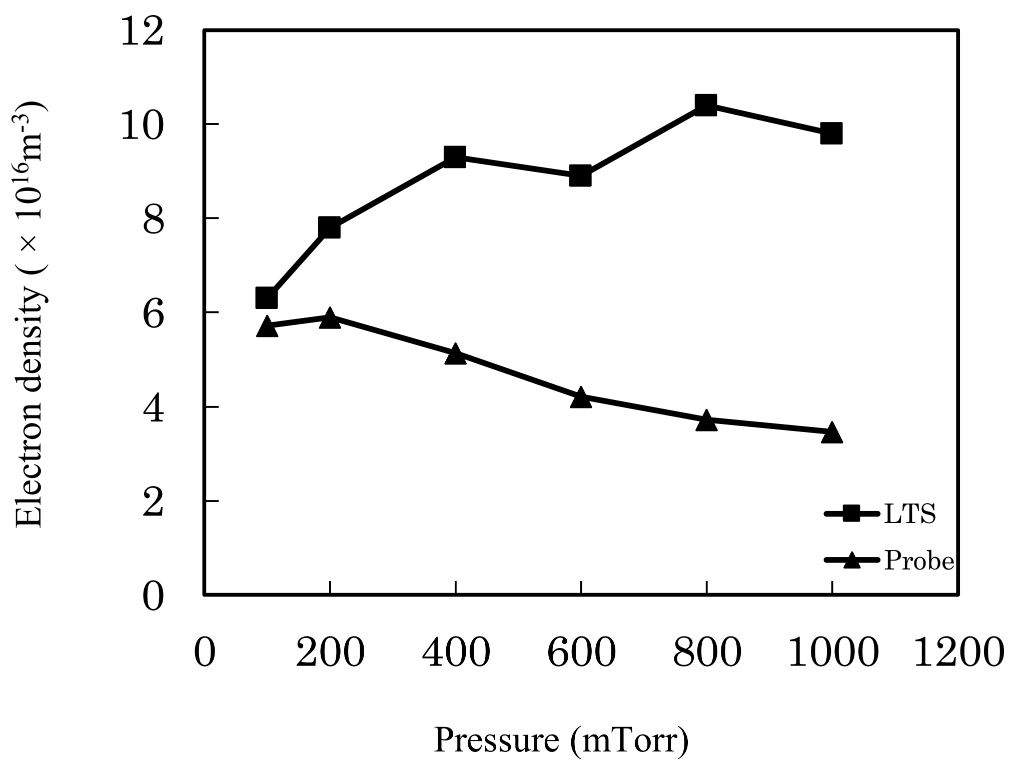

Fig. 4.5 Electron densities measured by the LTS method and Langmuir probe method for different gas pressures. Here the VHF power was fixed at 80 W.

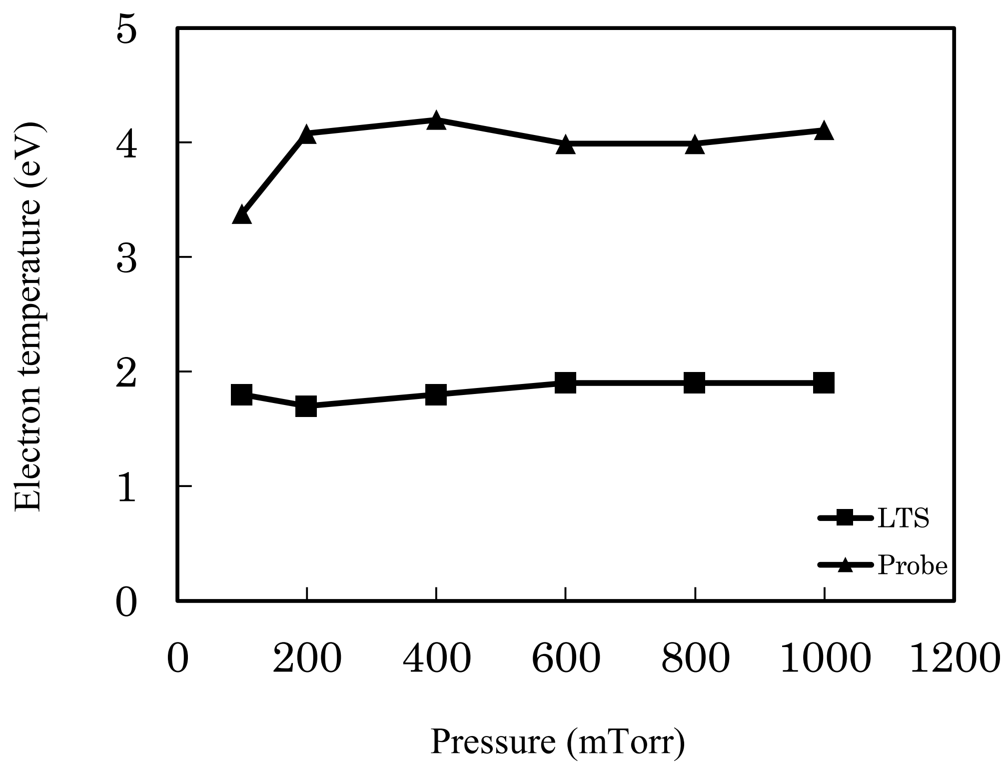

Fig. 4.6 Electron temperatures measured by the LTS method and Langmuir probe method for different gas pressures. Here the VHF power was fixed at 80 W.

4.2.2 Comparison of results by LTS method and probe method

Nishimiya [8] suggested the advantage of the balanced power feeding method, where the Langmuir probe was used as a diagnostic tool. In our previous study [6], we exmained the dependence of n_e and T_e by the LTS and Langmuir probe on the VHF power at the pressure of 100 mTorr. Recently there is a tendency operated at higher pressure in plasma processes to get higher deposition rates. In this paper, we investigated the characteristic of LTS method and Langmuir probe method at the gas pressrue higher than 100 mTorr. As seen in Fig. 4.5 and Fig. 4.6, when the gas pressure is 100 mTorr, n_e values measured by the LTS method and Langmuir probe method are 6.3×10^{16} m^{-3} and 5.7×10^{16} m^{-3}, respectively. The T_e value measured by LTS method is lower than that by probe method. This tendency agrees with the result reported in Ref. [8-9]. When the gas pressure is increased to 1000 mTorr, n_e measured by LTS method increased. On the contrary, n_e measured by the probe method decreases. This different tendency may due to the fact that the probe cannot be used at the higher gas pressure. Thus, we conclude that the LTS is a reliable diagnostic method at high gas pressures.

4.2.3 Simulation

We have performed the simulation of a VHF plasma by using the Plasma Hybrid Module (PHM) of PEGASUS software Inc. [10-11]. The detail of the PHM was described in Ref. [12]. Figure 4.7 shows the Balanced Power Feeding (BPF) model which uses a cylindrical coordinate system with axial symmetry. Here, we briefly describe the computational procedure of the PHM. The density and the velocity of electrons, which are utilized for the calculation of the electron energy distribution functions (EEDFs) by the Monte Carlo method, are calculated by the fluid model and the equation of the electron motion. A pair of parallel plate electrode with the radius of

34 mm was set at the center of a cylindrical chamber. The gap between the electrodes was fixed to 8 mm. The working gas was argon, the gas pressure used in this simulation was 100 mTorr and the amplitude of the applied voltages was in the range between 60 and 100 V. The argon gas was introduced from the centered top position of the chamber. An exhaust port was located on the bottom face of the chamber. The leak currents of the electrode are not considered in the model, thus, the effect of the applied VHF voltages in the BPF model on the VHF plasma with short-gap parallel electrodes was investigated.

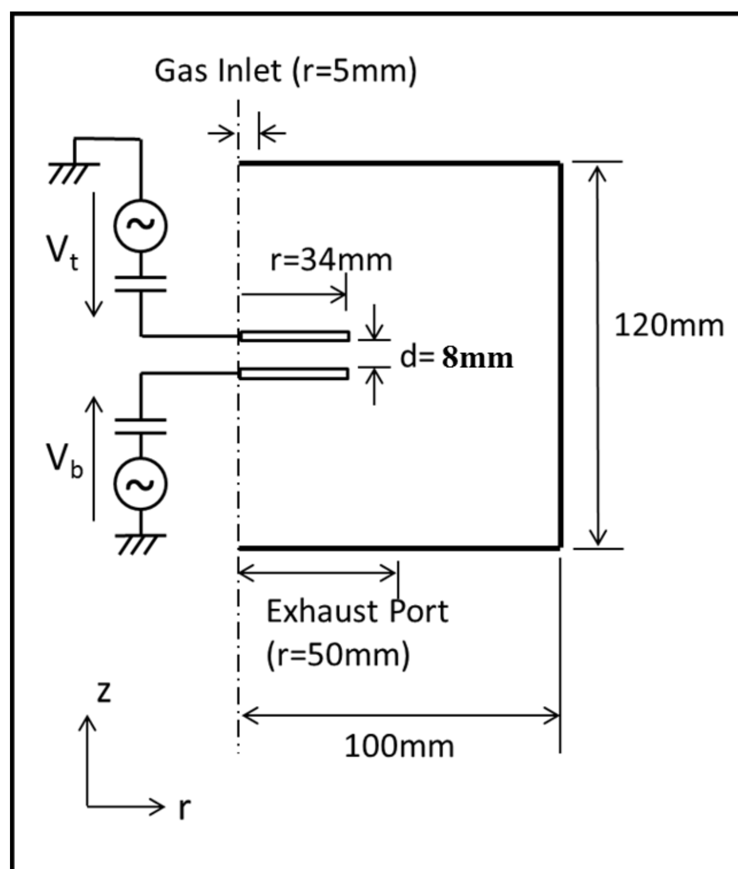

Fig. 4.7 Schematic diagram of BPF model.

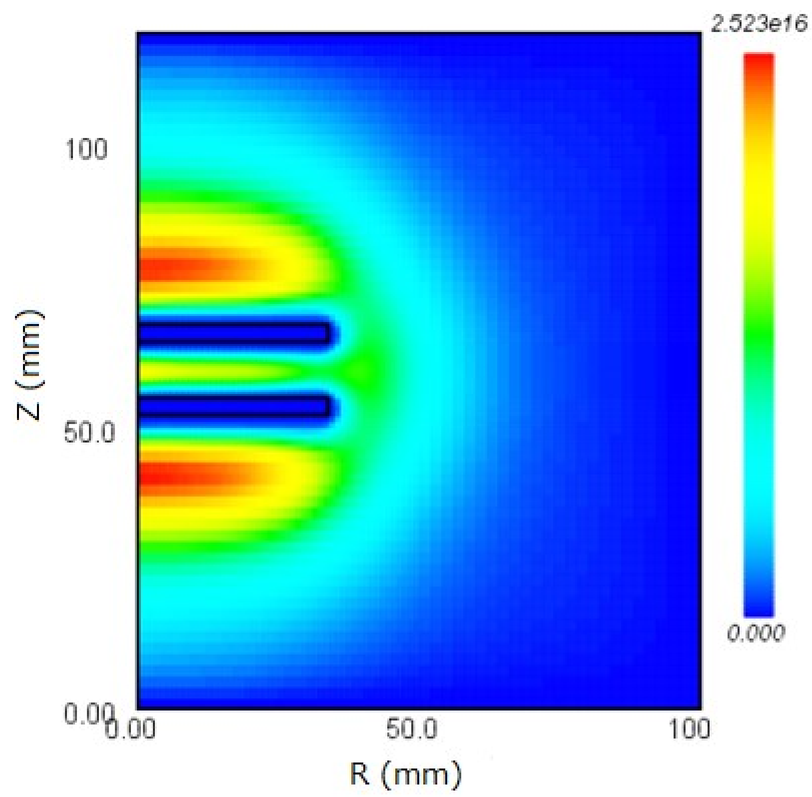

Fig. 4.8 Spatial distribution of the electron density at the gas pressure of 100 mTorr. The images are 2-D in the balanced power feeding model (V_{rf} = 60 V).

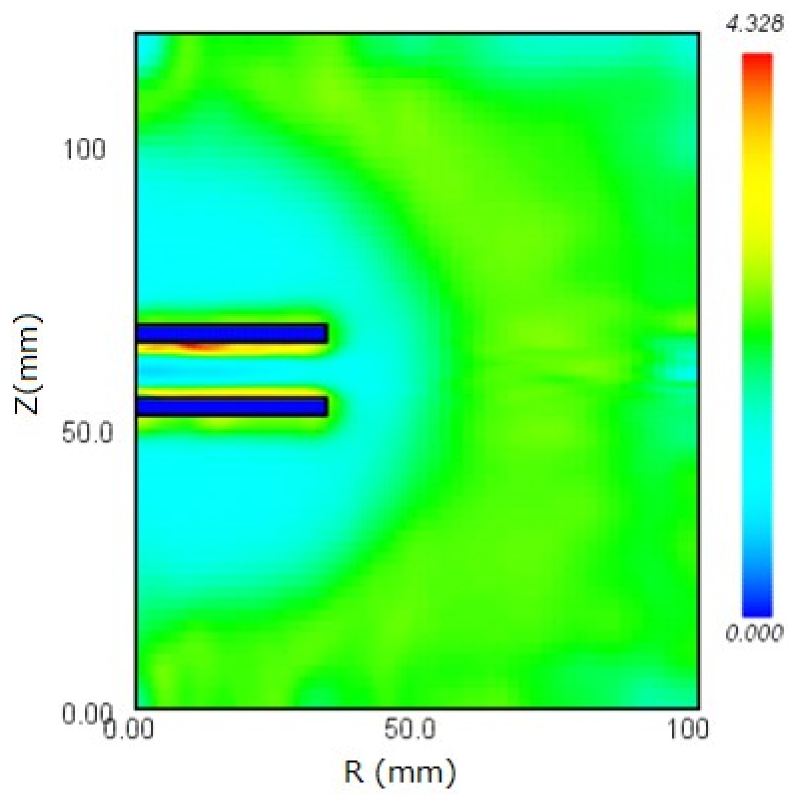

Fig. 4.9 Spatial distribution of the electron temperature at the gas pressure of 100 mTorr. The images are 2-D in the balanced power feeding model (V_{rf} = 60 V).

Figure 4.8 and Figure 4.9 show the 2-dimensional images of the electron density and the electron temperature in the BPF model. Here the frequency of the VHF power source and the amplitude of the VHF voltage are 60 MHz and 60 V, respectively. The gas pressure was set to 100 mTorr. The n_e and T_e values at the center of the electrodes in the BPF model are 1.5×10^{16} m^{-3} and 1 eV, respectively.

Figure 4.10 and Figure 4.11 demonstrate the applied voltage dependence of the n_e and T_e distributions. The distributions are in the z direction and are calculated at the radial position r = 20 mm. Obviously the highest n_e appears at the center position between two electrodes. The central n_e values for the applied voltage of 60 V, 80 V and 100 V are 1.5×10^{16} m^{-3}, 2.6×10^{16} m^{-3} and 4.1×10^{16} m^{-3}, respectively. In addition, T_e is kept around 1 eV at the center independent of the applied voltage. Besides, Fig. 4.10 and Fig. 4.11 show that the plasma is produced outside the discharge electrode and the n_e distribution outside the electrode takes a peak at z = 18 mm, namely 8 mm apart from the power electrode, and then, n_e decreases with the distance from the electrode. The VHF power of 20 W, 40 W, 60 W and 80 W in our experiment correspond to the V_{rf} of 28 V, 37 V, 45 V and 50 V, respectively. Therefore, we compared the measure plasma parameters obtained for the VHF power of 80 W with the calculated parameters by the simulation setting the applied voltage of 60 V. The n_e values obtained by the LTS method and the simulation model are 6.2×10^{16} m^{-3} and 1.5×10^{16} m^{-3}. On the other hand, T_e value obtained by the simulation model is 1 eV, and it is slightly lower than that by the LTS method. In any case, these results indicate that the plasma parameters obtained by the simulation are not so much different from those measured by the LTS method.

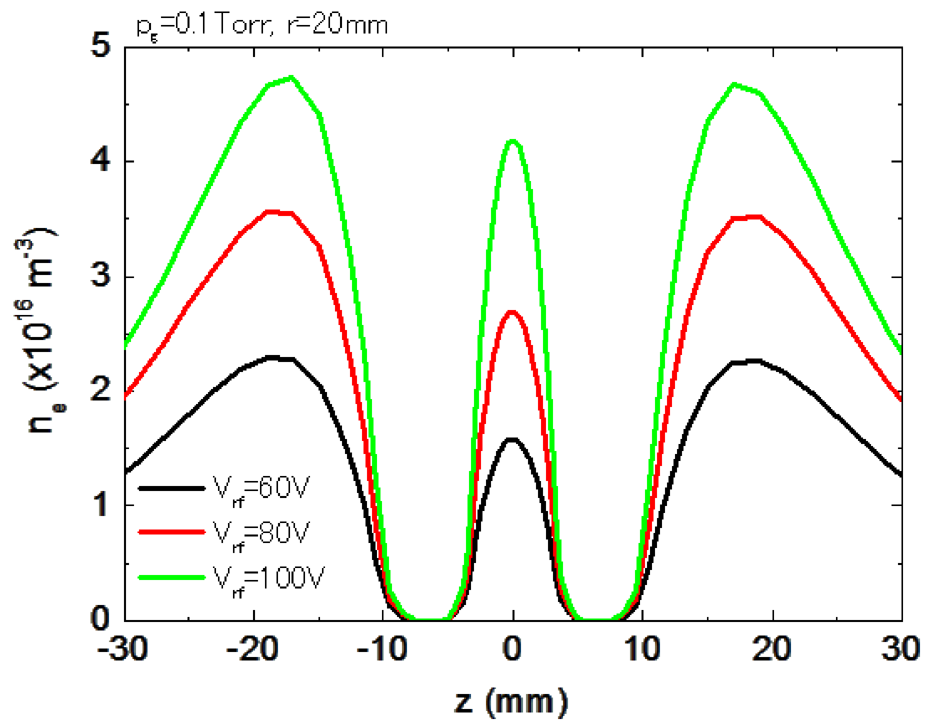

Fig. 4.10 Spatial distribution of the electron density for different applied voltages. The gas pressure was 100 mTorr, the distance of the electrodes was d = 8 mm. The distributions are in the z direction and are calculated at the radial position r = 20 mm.

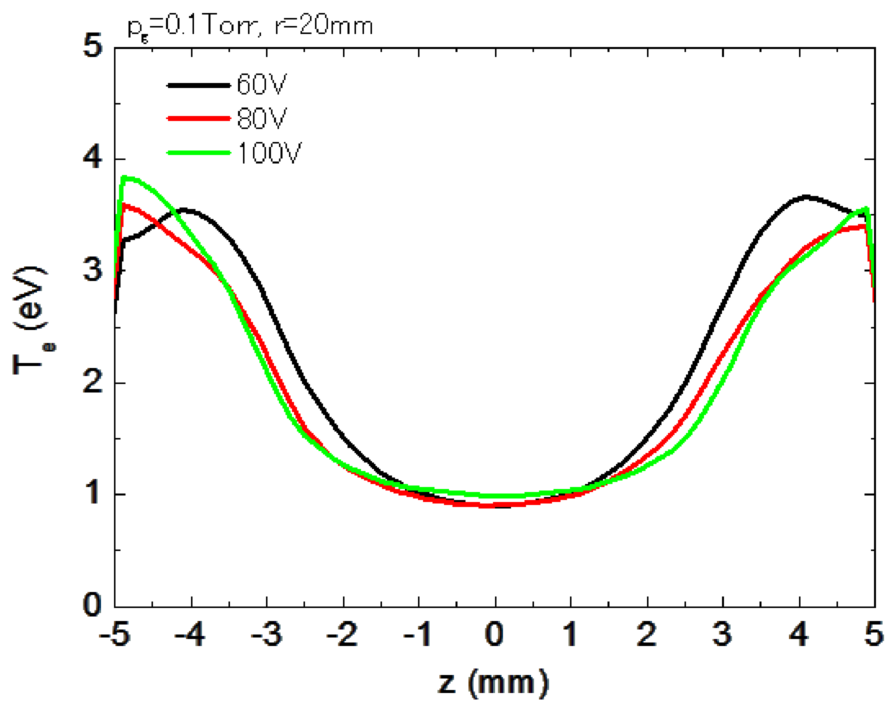

Fig. 4.11 Spatial distribution of the electron temperature for different applied voltages. The gas pressure was 100 mTorr, the distance of the electrodes was d = 8 mm. The distributions are in the z direction and are calculated at the radial position r = 20 mm.

4.3 Summary

We examined the dependence of the VHF plasma parameters on the gas pressure and the VHF power by using the LTS method. Here the VHF plasmas were generated by the balanced power feeding method and conventional power feeding method. Compared with the conventional power feeding method, n_e and T_e by the balanced power feeding method showed the outstanding performance not only on the pressure dependence but also on the power dependence. In addition, we measured the pressure dependence of the plasma parameters by LTS method and Langmuir probe method at high pressure that was reported as an indispensable condition for VHF plasma processes. It was found that as the gas pressure is increased from 100 mTorr to 1000 mTorr, the n_e values measured by the Langmuir probe method showed the different tendency from the values measured by the LTS method. This is considered that the Langmuir probe method is not reliable for high pressures at around 1 Torr.

We have successfully simulated the VHF argon plasma using the PHM of PEGASUS software. The 2-D spatial distributions of n_e and T_e indicate that the plasma is also produced outside the discharge electrode in the balanced power feeding model. The n_e and T_e values inside the electrodes in the BPF model are 1.5×10^{16} m^{-3} and 1 eV, and these values are not so much different from those measured by the LTS method. Thus, it is concluded that both LTS diagnostics and the simulation can be powerful tools to study VHF plasmas.

References

[1] Y. Yamauchi, Y. Takeuchi, H. Takatsuka, H. Yamashita, H. Muta and Y. Kawai, Contributions to Plasma Physics, 48, 4, 326 (2008).

[2] S. Y. Myong, K. Sriprapha, Y. Yashiki, S. Miyajima, A. Yamada and M. Konagai, Sol. Energy Mater. Sol. Cells, 92, 639 (2008).

[3] U. Graf, J. Meier, U. Kroll, J. Bailat, C. Droz, E. Vallat-Sauvain, A. Shah, Thin Solid Films, 427, 37 (2003).

[4] M. Isomura, M. Kondo and A. Matsuda, Jpn. J. Appl. Phys., 41, 1947 (2002).

[5] T. E. Sheridan and J. Goree, Phys. Fluids B, 3, 4, 326 (2008).

[6] W. Chen, K. Ogiwara, K. Koge, K. Tomita, K. Uchino, and Y. Kawai, to be published in Plasma and Fusion research.

[7] S. Hassaballa, M. Yakushiji, Y. Kim, K. Tomita, K. Uchino, and K. Muraoka, IEEE Trans. Plasma Sci. 32, 1 (2004).

[8] M.D. Bowden, M. Kogano , Y. Suetome. T. Hori, K.Uchino, and K. Muraoka, J. Vac. Sci. Technol. A 17, 493 (1999).

[9] M. Noguchi, T. Hirao, M. Shindo, K. Sakurauchi, Y. Yamagata, K. Uchino, Y. Kawai and K. Muraoka, Plasma Sources Sci. Technol. 12, 403 (2003).

[10] PEGASUS Software Inc., http://www.psinc.co.jp/english/index.html.

[11] Kushner M J, 2009 J. Phys. D: Appl. Phys., **42** 194013.

[12] K. Ogiwara, W. Chen, K. Uchino, K. Koge and Y. Kawai, to be published in Thin Solid Films.

Chapter 5
Conclusion

5.1 Summary of this study

In this study, the laser Thomson scattering (LTS) method was developed to diagnose very-high-frequency (VHF) argon plasmas. The VHF plasmas were produced between two parallel electrodes at high pressures, where a balanced power feeding was used to avoid anomalous discharges. Then, the characteristics of the VHF plasmas were clarified based on the measurements of plasma parameters by LTS. In addition, usefulness of the two-dimensional simulation for the study of VHF plasmas was examined. The achievements of this study are summarized as follows:

1. The LTS method was applied to measure the electron density n_e and electron temperature T_e of VHF argon plasmas. When the probing laser wavelength was 532 nm and the laser power density was ~10^{15} W/m^2, the Thomson scattering spectrum was obviously deformed by the effect of the photo-ionization of metastable argon atoms. The threshold laser power density at which the scattered light intensity from electrons in the plasma and that from electrons produced by photo-ionization are equivalent was found to be unexpectedly low (4×10^{13} W/m^2). To avoid the photo-ionization of metastable argon atoms, the laser power density was decreased to around 1×10^{13} W/m^2 by using a cylindrical lens as the focusing lens. Then, the n_e and T_e values measured by LTS and the probe method were compared for a VHF plasma using argon gas at a pressure of 100 mTorr. This comparison confirmed that the LTS method gave reasonable n_e and T_e values.

2. The dependences of the VHF plasma parameters on the gas pressure and power were examined by using the LTS method where the VHF plasma was generated by the balanced power feeding method and conventional power feeding method. Compared with the conventional power feeding method, n_e and T_e by the balanced power feeding method showed the outstanding performance not only on the pressure dependence but also on the power dependence. In addition, the pressure dependences of the plasma parameters were measured by the LTS method and the Langmuir probe method at high pressure that was reported as an indispensable condition on VHF plasma processes. It was found that as the gas pressure was changed in the range 100-1000 mTorr, the electron density measured by LTS method had the different tendency from that measured by the Langmuir probe method. This is considered to be due to the applicable limit of the Langmuir probe method.

3. The VHF argon plasma was simulated by using the Plasma Hybrid Module of PEGASUS software. The two-dimensional spatial distributions of n_e and T_e both inside and outside of the electrodes were successfully calculated using the balanced-power feeding-model. The values of n_e and T_e calculated inside the electrodes based on the balanced-power-feeding model is 1.5×10^{16} m^{-3} and 1 eV, and these values are close to those measured by the LTS method. Thus, it is concluded that both LTS diagnostics and the simulation can be powerful tools to study VHF plasmas.

5.2 Suggestions for the future work

In the future work, the diagnostics of a hydrogen plasma and a silane plasma will be the most attractive targets because they are used for the fabrication of the amorphous and microcrystalline silicon thin film solar cells.